UNIVERSITÀ DEGLI STUDI DI SALERNO

DIFARMA

UNIVERSITÀ DEGLI STUDI DI SALERNO
Dipartimento di Farmacia

PhD Program
in **Drug Discovery and Development**
XXXIII Cycle – Academic year 2020/2021

PhD Thesis in

Structural study of biomarkers for neurodegenerative diseases

Candidate

Angelo Santoro

Supervisor

Prof. *Anna Maria D'Ursi*

PhD Program Coordinator: Prof. *Gianluca Sbardella*

Lists of Publications

[1] Grimaldi, M.; Stillitano, I.; Amodio, G.; **Santoro, A.**; Buonocore, M., Moltedo, O.; Remondelli, P.; D'Ursi, A.M. Structural basis of antiviral activity of peptides from MPER of FIV gp36. *PLoS One*. [Online early access]. DOI: 10.1371/journal.pone.0204042 Published online Sep 21, 2018.

[2] Grimaldi, M.; Buonocore, M.; Scrima, M.; Stillitano, I.; D'Errico, G.; **Santoro, A.**; Amodio, G.; Eletto, D.; Gloria, A.; Russo, T.; Moltedo, O.; Remondelli, P.; Tosco, A.; Wienk, H.L.J..; D'Ursi, A.M. NMR Structure of the FIV gp36 C-Terminal Heptad Repeat and Membrane-Proximal External Region. *Int J Mol Sci.* **2020** 16;21(6):2037. DOI: 10.3390/ijms21062037

[3] Skaanning, L.K.; **Santoro, A.**; Skamris, T.; Martinsen, J.H.; D'Ursi, A.M.; Bucciarelli, S.; Vestergaard, B.; Bugge, K.; Langkilde, A.E.; Kragelund, B.B. The Non-Fibrillating N-Terminal of α-Synuclein Binds and Co-Fibrillates with Heparin. *Biomolecules.* **2020** Aug 16;10(8):1192. DOI: 10.3390/biom10081192.

[4] Castaldo. G.; Pagano, I.; Grimaldi, M.; Marino, C.; Molettieri, P.; **Santoro, A.**; Stillitano, I.; Romano, R.; Montoro, P.; D'Ursi, A.M.; Rastrelli, L. Effect of Very-Low-Calorie Ketogenic Diet on Psoriasis Patients: A Nuclear Magnetic Resonance-Based Metabolomic Study. *J Proteome Res.* **2020** Nov 9. DOI: 10.1021/acs.jproteome.0c00646.

[5] Buonocore, M.; Marino, C.; Grimaldi, M.; **Santoro, A.**; Firoznezhad, M.; Paciello, O.; Prisco, F.; D'Ursi, A.M. New putative animal reservoirs of SARS-CoV-2 in Italian fauna: A bioinformatic approach. *Heliyon.* **2020** Nov;6(11):e05430. DOI: 10.1016/j.heliyon.2020.e05430.

[6] Grimaldi, M.; Marino, C.; Buonocore, M.; **Santoro, A.**; Sommella, E.; Merciai, F.; Salviati, E.; De Rosa, A.; Nuzzo, T.; Errico, F.; Campiglia, P.; Usiello, A.; D'Ursi, AM. Prenatal and Early Postnatal Cerebral d-Aspartate Depletion Influences l-Amino Acid Pathways, Bioenergetic processes, and Developmental Brain Metabolism. *J Proteome Res.* **2021** Jan 1;20(1):727-739. DOI: 10.1021/acs.jproteome.0c00622.

Table of content

Abstract

The research activity of my PhD focused on the following topics:

- NMR conformational analysis of Aβ(1-42) in 50/50 HFIP/water v/v.
- Design and study the interaction of peptides from the binding site of antibodies targeting Aβ(1-42) epitopes.
- Study of interaction of heparin with α-synuclein$_{1-61}$ region.

Based on the amyloid-β (Aβ) cascade hypothesis, abnormal accumulation of the amyloid-β (Aβ) peptides into toxic extracellular plaques is the leading cause of neurodegeneration and dementia in Alzheimer's disease (AD) patients. The main components of the amyloid plaques are Aβ(1-40) and Aβ(1-42), soluble helical peptides that in overcoming toxic environmental conditions undergo a conformational transition to form β-sheet aggregates.

HFIP/water mixtures have been used as an excellent system to monitor the conformational changes induced in the stable Aβ(1-42) solution structure by increasing water amounts. Aβ(1-42) studied by NMR in 80/20 HFIP/water v/v mixture revealed regular helical-kink-helical structure, while in the mixture containing higher water content - 30/70 HFIP/water v/v mixture - it lost this structure, to assume a succession of β-bends conformations while conserving regular α-helix on ^{11}E-L^{17}.

The first part of my PhD project focused on the NMR study of Aβ(1-42) in 50/50 HFIP/water, a solvent mixture characterized by intermediate polarity compared to those previously used. Our data show that in these conditions, Aβ(1-42) is characterized by regular α-helix on ^{18}V-V^{24} residues, β-turns on ^{4}F-H^{14} and ^{32}I-G^{38} segments, short random coils, and bend structures on the remaining portions of the sequence. The C-terminus shows high flexibility and dynamic properties revealing a primary role in the transition to the β-strand conformation. Molecular dynamics simulations in water solution confirm that these flexible regions evolve to regular β-strand structures giving rise to a complex architecture of fibril β-sheet aggregates.

Based on the amyloid cascade hypothesis, hundreds of molecules have been tested, as possible AD therapeutics that can disaggregate Aβ fibrils or prevent their formation. More recently, the hypothesis has spread within the scientific community that immunotherapy targeting Aβ peptide has great potential for treating or preventing AD. Accordingly, several antibodies have been developed targeting different epitopes of Aβ(1-42). In this context, part of my research activity focused on the study of new peptides as possible ligands of Aβ(1-

42) designed on the model of the binding sites of different monoclonal antibodies. In particular, we selected solanezumab and crenezumab that bind ^{16}K-S^{26} and ^{13}H-D^{23} Aβ(1-42) segments and aducanumab that targets the ^{3}E-E^{11} N-terminal fragment. The designed peptides were studied for their interaction with Aβ(1-42) using CD and NMR spectroscopies; then, we studied their effect on the Aβ(1-42) aggregation using atomic force microscopy. Our data show that WAibH and SYSTPGK are endowed with an interesting ability to bind Aβ(1-42). Although characterized by a modest dissociation constant (K_D), they inhibit the formation of Aβ(1-42) mature fibrils, as shown by a quantitative decrease of fibrillation degree in AFM microscopy.

The research activity of my Ph.D. project carried out at the University of Copenhagen under the supervision of Prof. Birthe B. Kragelund was focused on the NMR study of the interaction of α-synuclein with glycosaminoglycans, in particular, heparin. The intrinsically disordered protein α-synuclein (aSN) is in its fibrillated state, the main component of Lewy bodies that are hallmarks of Parkinson's disease. Additional components include glycosaminoglycans, e.g. heparan sulfate proteoglycans. Heparan sulfate has, in an age-dependent matter, shown increased levels of sulfation. Heparin, a highly sulfated glycosaminoglycan, is a relevant mimic for heparan sulfate and has been shown to influence fibrillation of aSN.

In this context, using NMR experiments, I gave my contribution to demonstrate that a region corresponding to residues 1-61 of aSN lacks intrinsic fibrillation propensity, while fibrillation can be induced by heparin in a concentration-dependent manner. Structural shifts from disorder, via type I β-turns, to β-sheet, was observed in aSN_{1-61}. Therefore heparin can induce fibrillation of aSN_{1-61} as well as of the full aSN through weak binding to the N-terminal and the KTKE-motifs; it modulates the structure of aSN by inducing type I β-turn structures, which may be critical for triggering aSN fibrillation.

Introduction

1.1. Intrinsically disordered proteins (IDPs) and neurodegeneration

Intrinsically disordered proteins (IDPs) are unstructured proteins characterized by the lack of a single, well-defined three-dimensional structure and the ability to exist as heterogeneous ensembles of conformers.[1] The efficient sampling of a vast and heterogeneous conformational space endows them with enormous potential to interact with and control multiple binding partners simultaneously. Therefore, it was proposed that this structural plasticity is essential for a control role in weak regulatory networks (such as transcription regulation). In contrast to their stably folded counterparts, IDPs feature a rather flexible nature. It was demonstrated that there are significant differences between the amino acid sequences of IDPs/IDRs in comparison with structured globular proteins and/or domains. These differences are related to amino acid composition, hydrophobicity, aromaticity, sequence complexity, charge, flexibility, type and rate of amino acid substitutions.[2] In particular, IDPs' features are the low content of hydrophobic residues and the high presence of charged residues.[3] Another unique property of IDPs is to return to the highly flexible conformations after they have performed their biological function.[4] Moreover, in the literature, there are several pieces of evidence that demonstrated IDPs as highly prevalent in many genomes and involved in several processes, such as regulation of transcription and translation, cell cycle control, and signaling.[5] IDPs have a critical role in most important disease pathways, such as cancer, amyloidosis, diabetes, cardiovascular, and neurodegenerative diseases. It is predictable to affirm that changes in the environment or mutation of these molecules can affect their normal function, leading to misidentification and missignaling. More serious are the consequences of these dysfunctions, which lead to misfolding and aggregation. These processes are known to be associated with the pathogenesis of numerous diseases. Some IDPs, such as α-synuclein, tau protein, amyloid peptide, p53, and BRCA1, are important in neurodegenerative diseases and cancer, and as such, they represent attractive targets for drugs modulating protein-protein interactions. Indeed novel strategies for drug discovery have been developed based on IDPs.[2, 6] When errors occur at the IDPs protein-protein interaction, neurodegenerative disorders arise at the neuronal level.[1] These disorders are characterized by the progressive loss of neuron function associated with the aggregate deposition of misfolded IDP proteins.

IDP misfolded superstructures lose their native function and are toxic, inducing deregulation in the intracellular transport, degradation of the protein pathways, and alteration of vital cell functions.[7, 8] The misfolding and the presence of accumulation of deposits of

aggregates are especially common in neurodegenerative diseases such as Alzheimer's, Parkinson's, Huntington's, and prion diseases.[4, 9, 10]

The research activity related to my PhD project was focused on amyloid β-peptide (Aβ) and α-synuclein IDPs involved in Alzheimer's disease (AD) and Parkinson's disease (PD), respectively.

1.2. Amyloid β-peptide, Tau protein, and Alzheimer's Disease

Alzheimer's disease (AD) is a neurodegenerative disease responsible for slow and progressive brain cell destruction. AD is the most common form of dementia (representing about 50-80% of total cases).[11] Increasing evidence shows that it is related to the accumulation of neuro-fibrillar clusters, consisting of an abnormal amount of phosphorylated tau protein and the cerebral accumulation of extracellular senile plaques composed of an aggregated β-amyloid peptide (Aβ).[12] In the prodromal phase, neuropathological changes are observed in the temporal regions (hippocampus, parahippocampus, and cortex) and the area dedicated to long-term memory.[13] At the origin of the degenerative process, the β-amyloid peptide, depositing itself between neurons, acts as a glue, englobing large areas and giving rise to the formation of neuro-fibrillar plaques. As a consequence, the neuron cannot transmit nerve impulses. There are several hypotheses regarding the onset and degeneration of Alzheimer's disease. Neuropathological features of the disease include the presence of extracellular β amyloid consisting of deposits of the amyloid precursor (APP) and the formation of intracellular neuro-fibrillar clusters (NFT), dystrophic neuritis, and angiopathy amyloid dependent. Multiple hypotheses have been advanced to explain Alzheimer's disease etiology: genetic factors, hormonal, inflammatory, vascular, immunological factors, oxidative stress, dysfunctional calcium homeostasis, cell cycle dysregulations.

The amyloid cascade hypothesis [14] states that neurodegeneration in AD is caused by an abnormal accumulation of plaques made up of the β-amyloid peptide (Aβ) in various brain areas.[15] The plaques act by triggering a cascade that leads to the formation of neurofibrillary clusters causing neuronal injury. Amyloid peptides consist of 39-43 amino acid residues; they are the product of the proteolytical cleavage of APP mediated by the β- and γ-secretase. Inside the plaques, the Aβ peptides in β-sheet conformation assemble themselves, polymerizing in structurally different forms that include fibrillar and polymorphic oligomers.[15-17]

The environmental conditions are critical for Aβ peptide aggregation. The Aβ peptide is produced in soluble form but, in response to environmental factors, it aggregates in low

molecular weight soluble oligomers and high molecular weight proto oligomers fibrils (PFOs); these give rise to insoluble fibrils which form amyloid plaques.[15, 18, 19] For a long time, insoluble fibrils have been considered responsible for the onset of the disease, but actually, the correlation between insoluble fibrillar deposits and the manifestation of the disease is controversial. Recent evidence highlights the role of the oligomeric forms of the Aβ peptide to be the toxic species responsible for the AD onset.[20-23]

Many data show that the amyloid peptide's toxicity is triggered by cell membrane that causes misfolding and aggregation, while at the same time, amyloid oligomers cause increasing in permeability and the depletion of lipids from membranes.[24, 25]

1.3. α-synuclein and Parkinson's Disease

Synucleinopathies are a group of neurodegenerative diseases that includes Parkinson's disease (PD), dementia with Lewy bodies and multiple system atrophy. Histologically, all these pathologies are characterized by the presence of inclusions known as Lewy bodies and Lewy neurites composed of aggregated α-synuclein and located in the central nervous system (CNS).[26, 27] α-synuclein is encoded by the SNCA gene located on chromosome 4, region q21, and it is predominantly expressed in the brain, concentrating in nerve terminals. Synuclein is a family of proteins formed by three isoforms: α, β, and γ-synuclein.[28, 29] However, only the α isoform was found in Lewy bodies, suggesting that α-synuclein represents the main character in this neurodegenerative disease.

The α isoform structurally presents a single chain with 140 amino acids and displays 61% identity compared to β-synuclein (134 amino acids). It was demonstrated that α-synuclein maintains its disorder structure also in physiological cell conditions.[30] Upon reversible binding to negatively charged phospholipids, α-synuclein oligomerizes and undergoes structural changes to assume a highly dynamic α-helical conformation while still maintaining partially disordered stretches.[31, 32] This behavior is probably due to the presence in its sequence of seven imperfect repeats of eleven amino acids, each with a -KTKEGV- conserved core, which confer to the molecule several moieties rich in positively charged residues.[28] The native functions of the synucleins are not well established. However, α-synuclein is known to bind lipids, and subsequently, this complex was found in the plasma membrane of synaptic terminals and synaptic vesicles, suggesting a role in neurotransmitter release.[33] The misfolding of this complex may be one of the processes responsible for the pathology's onset since the lipid-bound α-synuclein leads to β-sheet rich amyloid fibrils, which was found as the main component of Lewy bodies and Lewy neurites.[10, 34] In contrast to its standard, physiological form, it was found that pathological

aggregated α-synuclein is extensively phosphorylated at ^{129}S and ^{87}S. Other posttranslational modifications present in pathological α-synuclein include nitration, oxidation, and truncation. In particular, the truncated α-synuclein, typically at its C-terminal, has shown an increased propensity towards fibrillation. There is a growing perception that soluble oligomeric forms of α-synuclein are the most relevant in terms of toxicity, suggesting that Lewy inclusions might represent a protective response and that interventions to favor the fibrillation process could be of therapeutic value.[35]

References

[1] Uversky VNJPS. A decade and a half of protein intrinsic disorder: biology still waits for physics. 2013;22:693-724.
[2] Uversky VN, Oldfield CJ, Dunker AKJARB. Intrinsically disordered proteins in human diseases: introducing the D2 concept. 2008;37:215-46.
[3] Uversky VN, Gillespie JR, Fink ALJPs, function,, bioinformatics. Why are "natively unfolded" proteins unstructured under physiologic conditions? 2000;41:415-27.
[4] Uversky VNJErop. Targeting intrinsically disordered proteins in neurodegenerative and protein dysfunction diseases: another illustration of the D2 concept. 2010;7:543-64.
[5] Wallin C, Luo J, Jarvet J, Wärmländer SK, Gräslund A. The Amyloid-β Peptide in Amyloid Formation Processes: Interactions with Blood Proteins and Naturally Occurring Metal Ions. Israel Journal of Chemistry. 2017;57:674-85.
[6] Uversky VN, Dunker AKJBeBA-P, Proteomics. Understanding protein non-folding. 2010;1804:1231-64.
[7] Uversky VNJFB. The triple power of D (3): protein intrinsic disorder in degenerative diseases. 2014;19:181-258.
[8] Kransnoslobodtsev AV, Shlyakhtenko LS, Ukraintsev E, Zaikova TO, Keana JF, Lyubchenko YLJNN, Biology, et al. Nanomedicine and protein misfolding diseases. 2005;1:300-5.
[9] Eftekharzadeh B, Hyman BT, Wegmann SJMoa, development. Structural studies on the mechanism of protein aggregation in age related neurodegenerative diseases. 2016;156:1-13.
[10] Breydo L, Uversky VNJM. Role of metal ions in aggregation of intrinsically disordered proteins in neurodegenerative diseases. 2011;3:1163-80.
[11] Abbott AJN. Dementia: a problem for our age. 2011;475:S2-S4.
[12] Joshi P, Benussi L, Furlan R, Ghidoni R, Verderio CJIjoms. Extracellular vesicles in Alzheimer's disease: friends or foes? Focus on aβ-vesicle interaction. 2015;16:4800-13.
[13] Tiraboschi P, Hansen L, Thal L, Corey-Bloom JJN. The importance of neuritic plaques and tangles to the development and evolution of AD. 2004;62:1984-9.
[14] Hardy J, Selkoe DJJs. The amyloid hypothesis of Alzheimer's disease: progress and problems on the road to therapeutics. 2002;297:353-6.
[15] Hardy JA, Higgins GAJS. Alzheimer's disease: the amyloid cascade hypothesis. 1992;256:184-6.
[16] Dickson DWJJoN, Neurology E. The pathogenesis of senile plaques. 1997;56:321-39.
[17] Selkoe DJJN. Translating cell biology into therapeutic advances in Alzheimer's disease. 1999;399:A23-A31.
[18] Kayed R, Pensalfini A, Margol L, Sokolov Y, Sarsoza F, Head E, et al. Annular protofibrils are a structurally and functionally distinct type of amyloid oligomer. 2009;284:4230-7.
[19] Kirschner DA, Abraham C, Selkoe DJJPotNAoS. X-ray diffraction from intraneuronal paired helical filaments and extraneuronal amyloid fibers in Alzheimer disease indicates cross-beta conformation. 1986;83:503-7.
[20] Harper JD, Wong SS, Lieber CM, Lansbury Jr PTJC, biology. Observation of metastable Aβ amyloid protofibrils by atomic force microscopy. 1997;4:119-25.
[21] Soto C, Castaño EM, Frangione B, Inestrosa NCJJoBC. The-helical to-strand transition in the amino-terminal fragment of the amyloid-peptide modulates amyloid formation. 1995;270:3063-7.
[22] Walsh DM, Klyubin I, Fadeeva JV, Cullen WK, Anwyl R, Wolfe MS, et al. Naturally secreted oligomers of amyloid β protein potently inhibit hippocampal long-term potentiation in vivo. 2002;416:535-9.
[23] Walsh DM, Hartley DM, Kusumoto Y, Fezoui Y, Condron MM, Lomakin A, et al. Amyloid β-protein fibrillogenesis: structure and biological activity of protofibrillar intermediates. 1999;274:25945-52.
[24] Lin H, Bhatia R, Lal RJTFJ. Amyloid β protein forms ion channels: implications for Alzheimer's disease pathophysiology. 2001;15:2433-44.
[25] Quist A, Doudevski I, Lin H, Azimova R, Ng D, Frangione B, et al. Amyloid ion channels: a common structural link for protein-misfolding disease. 2005;102:10427-32.
[26] Goedert M, Jakes R, Spillantini M. The synucleinopathies: twenty years on. J Parkinsons Dis 7: S51–S69. 2017.

[27] Spillantini MG, Crowther RA, Jakes R, Hasegawa M, Goedert MJPotNAoS. α-Synuclein in filamentous inclusions of Lewy bodies from Parkinson's disease and dementia with Lewy bodies. 1998;95:6469-73.
[28] Jakes R, Spillantini MG, Goedert MJFl. Identification of two distinct synucleins from human brain. 1994;345:27-32.
[29] Lavedan C, Leroy E, Dehejia A, Buchholtz S, Dutra A, Nussbaum RL, et al. Identification, localization and characterization of the human γ-synuclein gene. 1998;103:106-12.
[30] Theillet F-X, Binolfi A, Bekei B, Martorana A, Rose HM, Stuiver M, et al. Structural disorder of monomeric α-synuclein persists in mammalian cells. 2016;530:45-50.
[31] Ferreon ACM, Gambin Y, Lemke EA, Deniz AAJPotNAoS. Interplay of α-synuclein binding and conformational switching probed by single-molecule fluorescence. 2009;106:5645-50.
[32] Choi TS, Han JY, Heo CE, Lee SW, Kim HIJBeBA-B. Electrostatic and hydrophobic interactions of lipid-associated α-synuclein: The role of a water-limited interfaces in amyloid fibrillation. 2018;1860:1854-62.
[33] Fortin DL, Troyer MD, Nakamura K, Kubo S-i, Anthony MD, Edwards RHJJoN. Lipid rafts mediate the synaptic localization of α-synuclein. 2004;24:6715-23.
[34] Gai W, Yuan H, Li X, Power J, Blumbergs P, Jensen PJEn. In situ and in vitro study of colocalization and segregation of α-synuclein, ubiquitin, and lipids in Lewy bodies. 2000;166:324-33.
[35] Martinelli AH, Lopes FC, John EB, Carlini CR, Ligabue-Braun RJIjoms. Modulation of disordered proteins with a focus on neurodegenerative diseases and other pathologies. 2019;20:1322.

Chapter I: NMR solution structure of Aβ(1–42) peptide in HFIP/water 50/50

1. Introduction

Neurodegenerative diseases represent an increasingly common debilitating condition due to the current average lifespan. Among the neurodegenerative pathologies, Alzheimer's disease (AD) is one of the most studied.[1-3] This disorder is characterized, at the histological level, by the presence of neurofibrillary tangles and amyloid plaques mainly composed of 39-42 amino acid long peptides known as β amyloid peptides (Aβ). Aβ(1-40) and Aβ(1-42), deriving from a noncorrect cleavage of the transmembrane amyloid precursor protein (APP), are in a metastable equilibrium at the cell membrane interface. Here slight changes in the chemical-physical conditions - e.g., metal ions, pH, temperature - induce conformational transitions to form β-sheet structures evolving in starch-like amyloid fibrils.[4-6] The control of the β amyloid aggregation process as a therapeutic strategy for Alzheimer's disease has prompted the interest to investigate the conformation of the Aβ peptides, taking advantage of computational and experimental techniques. In particular, NMR spectroscopy has been extensively used to study the structure of Aβ(1-42) and its shorter fragments in several environmental conditions, where soluble helical structures are favored. Detergent micelles have been used to reproduce the cell membrane interface:[7-12] in SDS and LiDS micelles, the short Aβ(12-28), Aβ(25-35), and Aβ(1-28) fragments are arranged in regular α-helices[10, 11] while Aβ(1–40) shows an α-helical-kink-helical structure. This structural motif is conserved in Aβ(16-35) in mixed DPC/SDS micelles, where the stability of the structure depends on the charge of the micelle surface.[13] NMR analysis in an aqueous systems revealed that Aβ(1-40) forms a 3_{10} helix on ^{13}H-D^{23} residues and is unstructured in the N- and C-terminal regions.[7] On the other hand, Aβ(1–42) monomer contains ^{8}S-V^{24} and ^{28}K-V^{38} α-helices and a β-turn on ^{25}G-K^{28} residues.[14, 15]

Water/fluorinated alcohol mixtures have been used to solve Aβ(1-42)'s solution structure, thanks to the physical-chemical properties of the fluorinated solvents.[16] By tuning the proportion of HFIP and water components, different polarity systems have experimented, in which the conformations of Aβ(1-42) have been monitored. The NMR structure of Aβ(1-42) in HFIP/water 80/20 v/v is characterized by a stable structure including two, ^{8}S-G^{25} and ^{28}K-V^{38}, helical segments and a less regular ^{25}G-S^{26}, β-turn.[14] The NMR study of Aβ(1-42) in HFIP/water 30/70 v/v indicates the preservation of α-helix on ^{11}E-L^{17} and the presence of β-bends structures on the remaining parts of the sequence (**Figure 7C**).[17] CD experiments

using Aβ(1-42) in mixtures obtained by systematically changing the proportions of HFIP/water show that the 10/90 mixture is critical for a final shift to the β-sheet conformation, while the HFIP/water 50/50 mixture represents the condition where the first significant Aβ(1-42) conformational change occurs.[14]. Moreover, this condition was recently used in a protocol of amyloid fibrillation, where the evaporation of the solvent induced the formation of highly ordered Aβ(1-42) nanostructures.[18, 19]

In this context, the first part of my research activity was focused on the NMR study of Aβ(1-42) in HFIP/H_2O 50/50 v/v mixture. Conformational data acquired in these conditions fills the gap in knowing the different conformational states experimented by Aβ(1-42) moving from the α-helical to the β-sheet structure. Therefore, to validate our structure as representative of a starting condition for amyloid fibrils formation, we performed molecular dynamics simulations. The structure solved by us in the present study and compared to those previously solved in 80/20 and 30/70 HFIP/water indicates that the evolution of Aβ(1-42) from helical to the β-sheet structure follows unexpected routes. Moreover, it can be considered a valuable starting point to comprehend the key structural steps in the Aβ(1-42) transition from soluble α-helical to the β-sheet structure.

2. Results

2.1. NMR structure determination of Aβ(1-42) peptide

We expressed and purified a recombinant Aβ(1-42) peptide following the protocol of Walsh et al.[20], and we studied its conformation using solution NMR spectroscopy in mixed HFIP/water 50/50 v/v solvents. ^{1}H chemical shift assignment was carried out by iteratively analyzing 2D TOCSY and NOESY spectra using SPARKY software.[21] An overlook of the 1D proton spectra evidenced all the characteristics of a structured peptide, with 42 well-dispersed amide chemical shifts and uniform resonance line widths (**Figure 1**). The sequential chemical shift assignment was performed according to the Wüthrich procedure.[22]

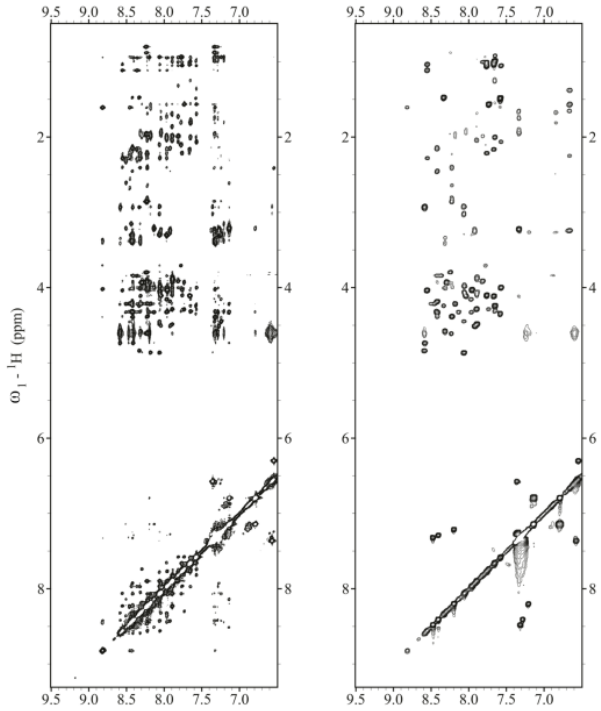

Figure 1. High field regions of 2D NOESY (left) and TOCSY (right) spectra of Aβ(1-42) acquired on Bruker 600 MHz NMR in HFIP/water 50/50 v/v.

Regular sequential and medium-range NOE effects, N,N(*i,i*+2), α,N(*i,i*+2), α,N(*i,i*+3) and α,β(*i,i*+3) were observed in 2D-NOESY spectrum collected in HFIP/water 50/50 v/v solution (summarized in the bar chart shown in **Figure 2A**). NOE patterns show regular secondary structures on the N-terminal and central region of Aβ(1-42) while consistent with the prevalence of flexible, unordered conformations on the C-terminal region. The Ramachandran plot shown in **Figure 2B** confirms these preliminary data.

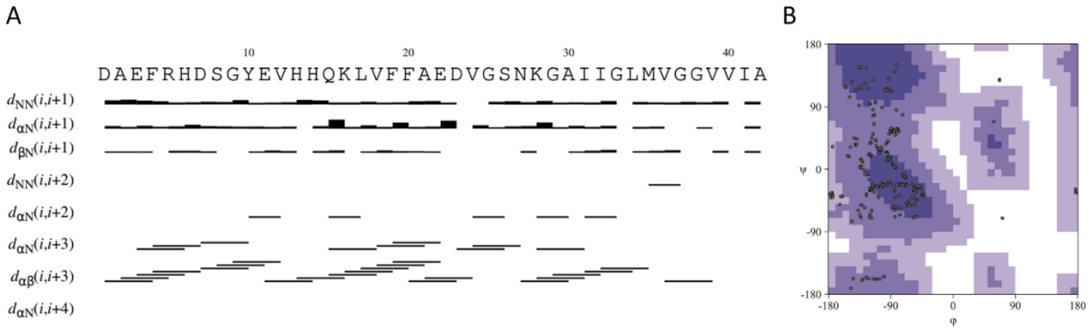

Figure 2. (A) Overview of the sequential and medium-range NOEs used to calculate the Aβ(1-42) peptide structure ensemble. **(B)** Ramachandran plot providing an overview of allowed and disallowed regions of torsion angle values.

The mentioned NOE data were translated into interprotonic distances using the CALIBA routine of CYANA 2.1 software[23] and then used as restraints for the NMR structure calculations. **Table 1** summarizes the statistics for the final NMR ensemble.[24]

Table 1. Statistics for the Structural Calculation of the NMR Ensemble of Aβ(1-42) peptide.

Number of experimental restraints after CYANA	
Total NOEs	585
Intra-residual	348
Sequential	143
Long-range	94
RMSD	
bb/heavy Å	2.92/3.11
Ramachandran analysis	
Favourable regions	50.60%
Additionally allowed regions	37.90%
Generously allowed regions	9.10%
Disallowed regions	2.4%

Figure 3 shows the bundle of the best 10 Aβ(1-42) NMR structures as derived from simulated annealing using CYANA software.[23] The structures, deposited on the Protein Data Bank with the accession code the PDB ID: **6SZF,** are overlapped on the backbone heavy atoms of ^{1}D-H^{14} N-terminal residues (RMSD 1.19 Å) and ^{15}Q-S^{26} central residues (RMSD 0.94 Å); on the contrary, as predicted from analysis of NOE data, the C-terminus is way more disordered and dynamic.

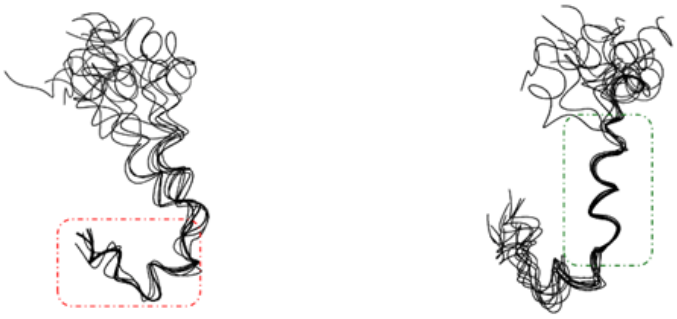

Figure 3. Bundles of the best 10 NMR structures of Aβ(1-42) derived from CYANA 2.1[23] based on NMR data acquired in HFIP/water 50/50 v/v. The structures are superimposed on the backbone heavy atoms of Aβ(1-42), N-terminal region ^{1}D-H^{14} (left), and central region ^{15}Q-S^{26} (right).

Figure 4 shows a ribbon representation of the most representative NMR structure of Aβ(1-42) acquired in HFIP/water 50/50 v/v. The *Define Secondary Structure of Proteins* (DSSP) plot calculated by GROMACS confirms the prevalence of regular α-helix conformations on

the ^{18}V to ^{24}V residues. Alternation of β-turn and bend conformations are observable at the N-terminal region.[25]

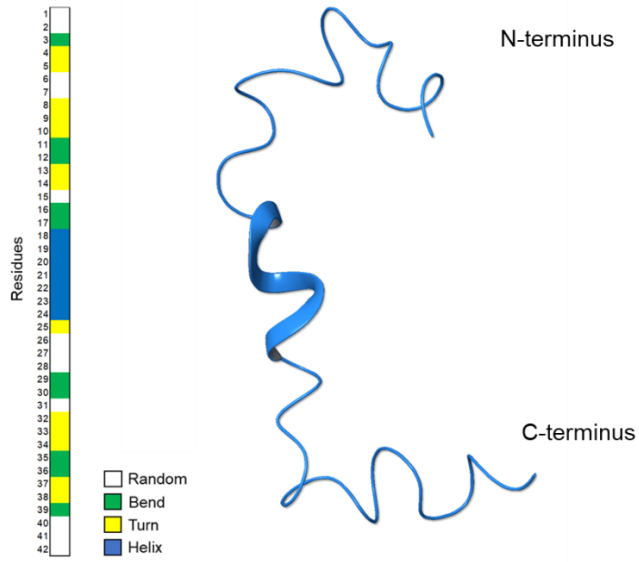

Figure 4. Ribbon representation of the most representative NMR structure of Aβ(1-42) acquired in HFIP/water 50/50 v/v. On the left, the *Define Secondary Structure of Proteins* (DSSP) plot calculated by GROMACS *do_dssp*.

2.2. Molecular Dynamics

To evaluate the stability of the Aβ(1-42) conformation solved in HFIP/water 50/50 v/v when exposed to a complete aqueous system, we performed MD simulations. Calculations were run with GROMACS.[25, 26] The best NMR structure based on the lowest value of the target function (CYANA 2.1)[23] was positioned in a box filled with explicit water for 50 ns at 300 K. As shown by the RMSD plot, the system reaches equilibrium after 1 ns and is stable during all the simulation (**Figure 5**).[27]

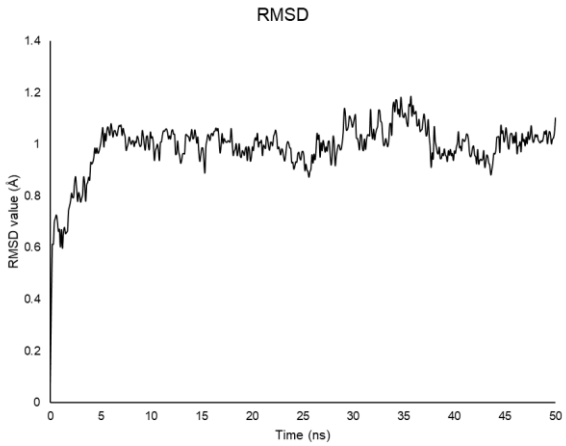

Figure 5. RMSD plot values for the backbone atoms of Aβ(1-42) throughout the 50 ns simulation as a function of time.

The snapshots of the 50 ns molecular dynamic trajectory of Aβ(1-42) in water are shown in **Figure 6**, overlapped to the solvent-accessible surface area plot. As reported, the ^{18}V-V^{24} α-helix slides to the ^{12}V-V^{18} region during the first steps of the dynamics experimenting unfolding after 40 ns. Remarkable is the β-sheet architecture formed at the ^{7}N-I^{41} C-terminus, which turns out to be extended to three strands within the 18 to 28 ns time range. Confirming data previously published,[28] this is a crucial step for the amyloid *seeding*, which is known to start in the neighbor of the ^{25}G-M^{35} residues. From 28.1 ns to the end of MD simulation, this strand gets confined in residues ^{35}M-V^{40,} indicating that the fibrillation is occurring, and the β-strand is transforming into a more complex intermolecular structure. Solvent accessible surface data (GROMACS *sasa*) (**Figure 6**) support this interpretation and show that N-terminal and central regions are equally exposed to the solvent until 40 ns when the central part has low solvent accessibility because shielded by the N-terminal segment.

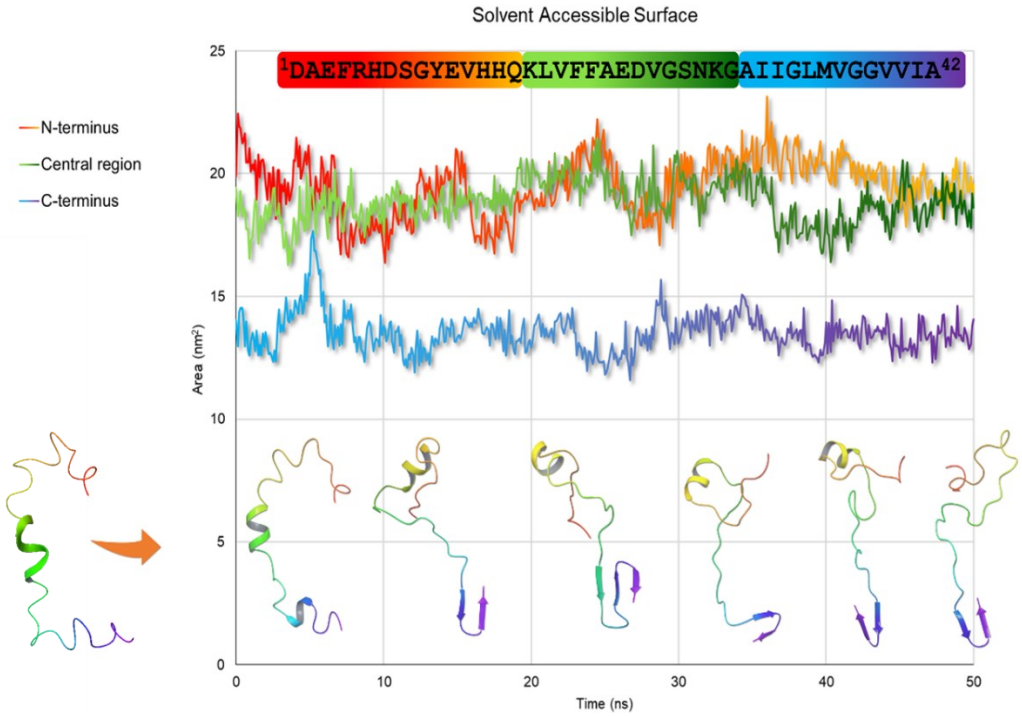

Figure 6. Snapshots of Aβ(1-42) trajectory throughout the 50 ns MD simulation in water superimposed to the solvent-accessible surface graph. The ribbons are colored in rainbow hue by atom position, from N-terminus (red) to C-terminus (purple). The solvent surface accessible area graph has been calculated by dividing the Aβ(1-42) peptide in three sections: N-terminus (residues ^{1}D-Q^{15}, red-to-yellow line), central region (residues ^{16}K-G^{29}, light green-to-dark green line), and C-terminus (residues ^{30}A-A^{42}, cyan-to-purple line).

3. Discussion

Based on the amyloid-β (Aβ) cascade hypothesis, abnormal accumulation of the amyloid-β (Aβ) peptides into toxic extracellular plaques is the leading cause of neurodegeneration and dementia in AD patients.[29-32] The main components of the amyloid plaques are Aβ(1-40) and Aβ(1-42), soluble helical peptides that in overcoming toxic environmental conditions undergo a conformational transition to form β-sheet oligomers, protofibrils, fibrils, and plaques.[31] How does this transition occurs is still questioned. Experimental data on this process mainly come from the solution NMR structure of the starting soluble conformation[14, 17] and the solid-state NMR structures of the final β-sheet structures.[33, 34] However, minimal experimental data are available on the conformers living the intermediate steps of helical-β-sheet transition. On the other hand, this is essential to identify the structural factors that are determinant for the transition.

HFIP/water mixtures have been used to solve the solution structure of Aβ(1-42), taking advantage of the fluorinated solvents' physical-chemical properties.[16] Moreover, this mixture was revealed to be an excellent system to monitor the conformational changes induced in the stable solution structure by increasing water amounts. In particular, Aβ(1-42) studied by NMR in 80/20 HFIP/water v/v mixture[14] revealed regular helical-kink-helical structure, while in the mixture containing higher water content - 30/70 HFIP/water v/v mixture - it is arranged in a succession of β-bends (**Figure 7C**) while conserving regular α-helix on ^{11}E-L^{17}.

Part of the research activity of my PhD project focused on the NMR study of Aβ(1-42) in - 50/50 HFIP/water, a solvent mixture characterized by intermediate polarity compared to those previously used. NMR data show that Aβ(1-42) in 50/50 HFIP/water is characterized by regular α-helix on ^{18}V-V^{24} residues, β-turns on ^{4}F-H^{14} and ^{32}I-G^{38} segments, short random coils, and bend structures on the remaining portions of the sequence (**Figure 7B**). According to an ideal scale of structure regularity and stability, this structure, compared to those previously solved, shows intermediate properties between the prevalent α-helix calculated in HFIP/water 80/20 and the prevalent bend calculated in HFIP/water 30/70.

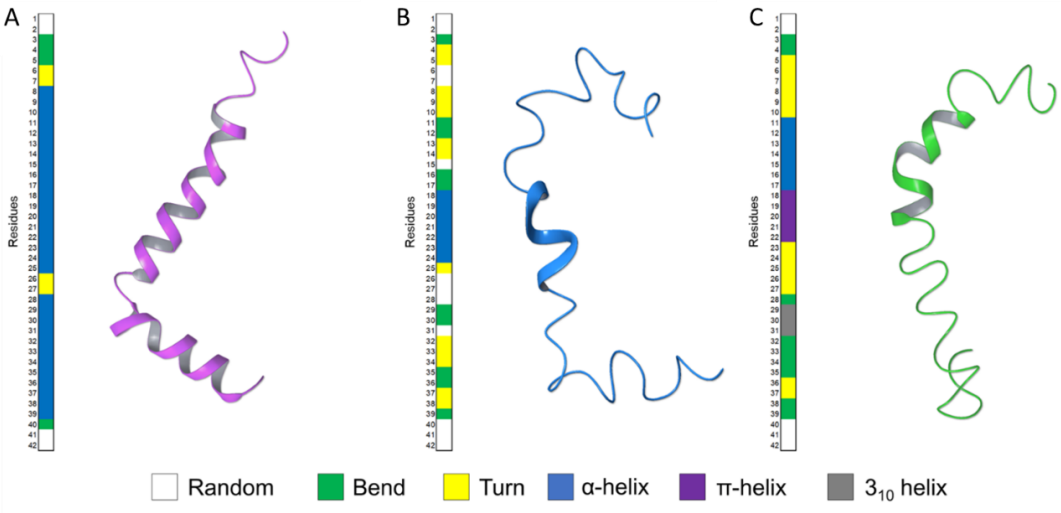

Figure 7. Comparison of the Aβ(1-42) structures in the different solvent system of HFIP/water v/v, **A)** 80/20 (PDBID: 1IYT); **B)** 50/50 (PDBID: 6SZF); **C)** 30/70 (PDBID: 1Z0Q).

However, by comparing the localization of the helical segments in the three structures, we can argue that moving from 80/20 to 30/70 HFIP/water condition, the transition to a more extended structure is not merely the result of helices unfolding, may occur through the sliding of single pieces of the secondary structures to the various parts of the sequence.

By looking at the dynamic properties of Aβ(1-42) in the 80/20, 30/70, and 50/50 HFIP/water v/v conditions, we can affirm that C-terminal is flexible and highly dynamic. To investigate the consequences of this structural property in water, we performed 50 ns molecular dynamic simulations. Snapshots of Aβ(1-42) trajectory throughout MD simulation and solvent accessible surface plot indicate that the ^{18}V-V^{24} α-helix slides to residues ^{12}V-V^{18} within the first steps, to be unfolded in the last steps of the dynamic. Starting from ^{25}G-M^{35} segment, a β-sheet architecture in the C-terminus is built up, including ^{27}N-I^{41}. This is involved in a complex intermolecular structure, as shown by the low solvent accessibility of the ^{35}M-V^{40} strand, that during the last step of the dynamic is involved in intermolecular interaction to form fibril aggregate structures.

4. Conclusions

We have studied the conformation of Aβ(1-42) in 50/50 HIFIP/water v/v solvent. This mixture represents an intermediate condition between those previously explored represented by apolar 80/20 HFIP/water and polar 30/70 HFIP/water. The structure solved by us provides a snapshot of the Aβ(1-42) conformations occurring during the helical-β sheet transition: the starting condition's helical structure loses its regularity and slides to the central region, known as critical for amyloid seeding. The C-terminus shows high flexibility and dynamic

properties revealing a primary role in the transition to the β-strand conformation. Indeed, molecular dynamic simulations in water solution confirm that these flexible regions evolve to regular β-strand structures giving rise to a complex architecture of fibril β-sheet aggregates.

5. Materials and Methods

5.1. Aβ(1-42) peptide production

Aβ(1-42) peptide was obtained after transformation of *E.Coli* BL21(DE3)-pLysS cells with PetSac plasmid provided by the research group of Walsh.[20] To optimize expression levels, were used *E. Coli*, Ca^{2+}-competent (BL21(DE3)-pLysS) cells obtained by thermal shock and allowed to grow in agar plates containing the LB culture medium with ampicillin (50 mg/L). The individual colonies were taken from a stock solution, stored at a temperature of -80 °C, and added to 50 mL of preinoculum, where 50 μL of ampicillin (50 mg/L) was previously added. The preparation was left in a thermostatic incubator, under constant stirring, at a temperature of 37 °C for the overnight. The following day, 5 mL of the culture was transferred to 500 mL of LB medium added with 500 μL of ampicillin (50 mg/L). When bacterial clones reached a final OD_{600} of 0.6 at 37°C, was added 50mg/L of isopropyl-thio-β-D-galactoside (IPTG). The cells were collected after 4 h of induction and centrifuged to remove the fraction constituted by the supernatant. Subsequently, the resulting pellet was thawed and sonicated three times in a solution containing: Tris/HCl pH 8.0 and EDTA, at a concentration of 10 mM and 1 mM respectively, for 5 minutes on ice (1/2 horn, 50% duty cycle). The sonicate was centrifuged for 10 minutes at 8000 rcf. The supernatant was removed, and the pellet was resuspended in a solution containing: 8 M urea, Tris/HCl pH 8.0 10 mM, EDTA 1 mM and sonicate as before. The resulting solution, containing Aβ(1-42) in the urea-soluble inclusion bodies, was diluted with a 10 mM Tris/HCl solution pH 8.0 and 1 mM EDTA. Subsequently, the solution was purified with a HiTrap® column, at a flow rate of 1 mL/min, using an AKTA purification system. The protein was eluted with an elution buffer (8 M urea, Tris/HCl pH 8.0 10 mM, 1 mM EDTA, 1 M NaCl). The eluted fraction was subsequently dialysed against Tris/HCl pH 8.0 10 mM and freeze-dried. The purity of the peptide was verified using the SDS-PAGE electrophoretic technique, electrophoresis on polyacrylamide gel (PAGE) in the presence of sodium dodecyl sulphate (SDS), using Coomassie Blue Staining. The SDS-PAGE electrophoresis of the previously sonicated cell pellet revealed that the majority of Aβ(1-42) was present in the band between 4 and 5 kDa. In order to support the peptide expression, the MALDI (Matrix-Assisted Laser Desorption/Ionization) mass spectrometry technique was used. The sample was previously

dried and placed in a MALDI sample support consisting of a solution matrix (4-hydroxy acid, α-cyanic cinnamic, 25 mM citric acid), which favours the crystallization of the compounds and allows an optimal analysis.

5.2. NMR sample preparation

Aβ(1-42) peptide has a very high tendency to form fibrils. To preserve the peptide in the monomeric form and avoid the formation of oligomeric and polymeric forms, before and during the experiments, Aβ(1-42) was subjected to a defibrillating treatment following the procedure described by Jao et al.[35] The Aβ(1-42) peptide was dissolved in trifluoroacetic acid (TFA) until complete solubilization of the powder sample and left in TFA for 3 h. Subsequently, the TFA was removed under nitrogen flow and was diluted 10-fold with milliQ water and lyophilized. This procedure was adopted for NMR analysis immediately before dissolution in the appropriate solvent.

5.3. NMR spectroscopy

5.3.1. Spectra acquisition

NMR spectra were recorded on a Bruker DRX-600 spectrometer. Aβ(1-42) peptide (500 μM) was dissolved in HFIP/water-D_2O 50/50 v/v. 1D ^1H homonuclear spectrum was recorded in the Fourier mode, with quadrature detection. 2D ^1H homonuclear TOCSY, NOESY experiments were run in the phase-sensitive mode using quadrature detection in ω1 by time-proportional phase incrementation of the initial pulse.[36-38] The water signal was suppressed by excitation sculpting experiments.[39] Before Fourier transformation, the time domain data matrices were multiplied by shifted $\sin^2$ functions in both dimensions. A mixing time of 80 ms was used for the TOCSY experiments. NOESY experiments were run at 298 K with mixing times of 200 ms.

5.3.2. Assignment of NMR resonances

The assignment of chemical shifts was obtained by the usual approach described by Wuthrich[22] examining 2D TOCSY and NOESY spectra using SPARKY software.[21] Intramolecular distance restraints derived from nuclear overhauser enhancements (NOEs) were obtained from the 2D NOESY spectrum recorded on a 600 MHz spectrometer.

5.3.3. Structure calculation

Peak volumes were translated into upper distance bounds with the CALIBA routine from the CYANA 2.1 software package.[23] After discarding redundant and duplicated constraints, the final list of constraints was used to generate an ensemble of 50 structures by

the standard CYANA protocol of simulated annealing in torsion angle space (using 6000 steps). The entries that present the lowest target function value (0.83-1.19) and small residual violations (maximum violation=0.38 Å) were analysed using the PyMOL program.[40]

5.4. Molecular dynamics

Molecular Dynamics (MD) simulations on Aβ(1-42) structure obtained from CYANA calculations were performed with GROMACS,[25, 26] by using Gromos96 53a6 force field.[41] The simulations were run for 50 ns at 300 K. The structure was immersed in explicit water using the SPC model.[42] The protein was solvated and the system was neutralized by adding 3 Na^+ ions. After these steps, the energy minimization of the system was performed and then the system was equilibrated using NVT and NPT runs. The temperature and pressure of the system were kept constant at 300 K and 1.01325 bar using the Berendsen weak coupling-method.[42, 43] The results were used for a 50 ns MD simulation using Particle Mesh Ewald for long range electrostatics under NPT conditions.[44] Coordinates were saved every 50000 steps. Trajectory file was fitted in the box and converted in PDB coordinates by using *trjconv* tool of GROMACS Package. The structure was visualized with Maestro by Schrödinger.[45] Root mean square deviation (RMSD) of peptide backbone was calculated using *rms* tool of GROMACS and plotted using R (version 3.6.0).[46] Ramachandran plot was calculated using *rama* tool of GROMACS. Solvent accessible surface plot was calculated using *sasa* tool of GROMACS. Define Secondary Structure of Proteins (DSSP) plot was calculated using *do_dssp* tool of GROMACS.

References

[1] Goyal D, Shuaib S, Mann S, Goyal B. Rationally designed peptides and peptidomimetics as inhibitors of amyloid-β (Aβ) aggregation: potential therapeutics of Alzheimer's disease. ACS combinatorial science. 2017;19:55-80.

[2] De-Paula VJ, Radanovic M, Diniz BS, Forlenza OV. Alzheimer's disease. Subcell Biochem. 2012;65:329-52.

[3] Prince M, Bryce R, Albanese E, Wimo A, Ribeiro W, Ferri CP. The global prevalence of dementia: a systematic review and metaanalysis. Alzheimer's & dementia. 2013;9:63-75. e2.

[4] Selkoe DJ, Hardy J. The amyloid hypothesis of Alzheimer's disease at 25 years. EMBO molecular medicine. 2016;8:595-608.

[5] Kang J, Lemaire H-G, Unterbeck A, Salbaum JM, Masters CL, Grzeschik K-H, et al. The precursor of Alzheimer's disease amyloid A4 protein resembles a cell-surface receptor. Nature. 1987;325:733-6.

[6] Zou K, Gong J-S, Yanagisawa K, Michikawa M. A novel function of monomeric amyloid β-protein serving as an antioxidant molecule against metal-induced oxidative damage. Journal of Neuroscience. 2002;22:4833-41.

[7] Coles M, Bicknell W, Watson AA, Fairlie DP, Craik DJJB. Solution Structure of Amyloid β-Peptide (1− 40) in a Water− Micelle Environment. Is the Membrane-Spanning Domain Where We Think It Is? 1998;37:11064-77.

[8] Shao H, Jao S-c, Ma K, Zagorski MGJJomb. Solution structures of micelle-bound amyloid β-(1-40) and β-(1-42) peptides of Alzheimer's disease. 1999;285:755-73.

[9] Jarvet J, Damberg P, Bodell K, Göran Eriksson L, Graeslund AJJotACS. Reversible random coil to β-sheet transition and the early stage of aggregation of the Aβ (12− 28) fragment from the Alzheimer peptide. 2000;122:4261-8.

[10] Talafous J, Marcinowski KJ, Klopman G, Zagorski MGJB. Solution Structure of Residues 1-28 of the Amyloid. beta.-Peptide. 1994;33:7788-96.

[11] Kohno T, Kobayashi K, Maeda T, Sato K, Takashima AJB. Three-dimensional structures of the amyloid β peptide (25− 35) in membrane-mimicking environment. 1996;35:16094-104.

[12] Fletcher TG, Keire DAJPs. The interaction of β-amyloid protein fragment (12-28) with lipid environments. 1997;6:666-75.

[13] Grimaldi M, Scrima M, Esposito C, Vitiello G, Ramunno A, Limongelli V, et al. Membrane charge dependent states of the β-amyloid fragment Aβ (16–35) with differently charged micelle aggregates. 2010;1798:660-71.

[14] Crescenzi O, Tomaselli S, Guerrini R, Salvadori S, D'Ursi AM, Temussi PA, et al. Solution structure of the Alzheimer amyloid β-peptide (1–42) in an apolar microenvironment: Similarity with a virus fusion domain. European Journal of Biochemistry. 2002;269:5642-8.

[15] Janek K, Rothemund S, Gast K, Beyermann M, Zipper J, Fabian H, et al. Study of the conformational transition of Aβ (1− 42) using d-amino acid replacement analogues. 2001;40:5457-63.

[16] Österlund N, Luo J, Wärmländer SK, Gräslund AJBeBA-P, Proteomics. Membrane-mimetic systems for biophysical studies of the amyloid-β peptide. 2019;1867:492-501.

[17] Tomaselli S, Esposito V, Vangone P, van Nuland NA, Bonvin AM, Guerrini R, et al. The α-to-β conformational transition of Alzheimer's Aβ-(1–42) peptide in aqueous media is reversible: a step by step conformational analysis suggests the location of β conformation seeding. ChemBioChem. 2006;7:257-67.

[18] Pachahara SK, Chaudhary N, Subbalakshmi C, Nagaraj RJJoPS. Hexafluoroisopropanol induces self-assembly of β-amyloid peptides into highly ordered nanostructures. 2012;18:233-41.

[19] Pachahara SK, Adicherla H, Nagaraj RJPO. Self-Assembly of Aβ40, Aβ42 and Aβ43 peptides in aqueous mixtures of fluorinated alcohols. 2015;10:e0136567.

[20] Walsh DM, Thulin E, Minogue AM, Gustavsson N, Pang E, Teplow DB, et al. A facile method for expression and purification of the Alzheimer's disease-associated amyloid β-peptide. The FEBS journal. 2009;276:1266-81.

[21] Goddard T, Kneller D. SPARKY 3. University of California, San Francisco. 2004;15.

[22] Wüthrich K. NMR with proteins and nucleic acids. Europhysics News. 1986;17:11-3.

[23] Guntert P. Automated NMR structure calculation with CYANA. Methods in molecular biology (Clifton, NJ). 2004;278:353-78.
[24] Dongre R, Folkers GE, Gualerzi CO, Boelens R, Wienk H. A model for the interaction of the G3-subdomain of Geobacillus stearothermophilus IF2 with the 30S ribosomal subunit. Protein Science. 2016;25:1722-33.
[25] Abraham MJ, Murtola T, Schulz R, Páll S, Smith JC, Hess B, et al. GROMACS: High performance molecular simulations through multi-level parallelism from laptops to supercomputers. SoftwareX. 2015;1:19-25.
[26] Bekker H, Berendsen H, DIJKSTRA E, Achterop S, van Drunen R, der Spoel D, et al. Gromacs: A parallel computer for molecular dynamics simulations. 1993.
[27] Safarizadeh H, Garkani-Nejad Z. Molecular docking, molecular dynamics simulations and QSAR studies on some of 2-arylethenylquinoline derivatives for inhibition of Alzheimer's amyloid-beta aggregation: Insight into mechanism of interactions and parameters for design of new inhibitors. Journal of Molecular Graphics and Modelling. 2019;87:129-43.
[28] Iadanza MG, Jackson MP, Hewitt EW, Ranson NA, Radford SE. A new era for understanding amyloid structures and disease. Nature Reviews Molecular Cell Biology. 2018;19:755-73.
[29] Schenk DJNRN. Amyloid-β immunotherapy for Alzheimer's disease: the end of the beginning. 2002;3:824-8.
[30] Selkoe DJ, Hardy JJEmm. The amyloid hypothesis of Alzheimer's disease at 25 years. 2016;8:595-608.
[31] Ahmed M, Davis J, Aucoin D, Sato T, Ahuja S, Aimoto S, et al. Structural conversion of neurotoxic amyloid-β 1–42 oligomers to fibrils. Nature structural & molecular biology. 2010;17:561.
[32] Rosenberg RN, Lambracht-Washington D, Yu G, Xia W. Genomics of Alzheimer disease: a review. JAMA neurology. 2016;73:867-74.
[33] Xiao Y, Ma B, McElheny D, Parthasarathy S, Long F, Hoshi M, et al. Aβ (1–42) fibril structure illuminates self-recognition and replication of amyloid in Alzheimer's disease. Nature structural & molecular biology. 2015;22:499-505.
[34] Colvin MT, Silvers R, Ni QZ, Can TV, Sergeyev I, Rosay M, et al. Atomic resolution structure of monomorphic Aβ42 amyloid fibrils. 2016;138:9663-74.
[35] Jao S-C, Ma K, Talafous J, Orlando R, Zagorski MG. Trifluoroacetic acid pretreatment reproducibly disaggregates the amyloid β-peptide. Amyloid. 1997;4:240-52.
[36] Bax A, Davis DG. MLEV-17-based two-dimensional homonuclear magnetization transfer spectroscopy. J Magn Reson 1985;65:355-60.
[37] Jeener J, Meier B, Bachmann P, Ernst R. Investigation of exchange processes by two-dimensional NMR spectroscopy. J Chem Phys. 1979;71:4546-53.
[38] Piantini U, Sorensen O, Ernst RR. Multiple quantum filters for elucidating NMR coupling networks. JACS. 1982;104:6800-1.
[39] Parella T, Adell P, Sánchez-Ferrando F, Virgili A. Effective multiple-solvent suppression scheme using the excitation sculpting principle. Magnetic resonance in chemistry. 1998;36:245-9.
[40] DeLano WL. Pymol: An open-source molecular graphics tool. CCP4 Newsletter on protein crystallography. 2002;40:82-92.
[41] Oostenbrink C, Villa A, Mark AE, Van Gunsteren WF. A biomolecular force field based on the free enthalpy of hydration and solvation: the GROMOS force-field parameter sets 53A5 and 53A6. Journal of computational chemistry. 2004;25:1656-76.
[42] Berendsen HJ, Postma JP, van Gunsteren WF, Hermans J. Interaction models for water in relation to protein hydration. Intermolecular forces: Springer; 1981. p. 331-42.
[43] Bussi G, Donadio D, Parrinello M. Canonical sampling through velocity rescaling. The Journal of chemical physics. 2007;126:014101.
[44] Onufriev A, Case DA, Bashford D. Effective Born radii in the generalized Born approximation: the importance of being perfect. Journal of computational chemistry. 2002;23:1297-304.
[45] Schrödinger. Maestro. New York, NY: LLC; 2020.
[46] Team RC. R: A language and environment for statistical computing. 2013.

Chapter II: Peptides from anti-Aβ(1-42) antibodies

1. Introduction

Several therapeutic approaches to control Alzheimer's disease (AD) are based on the control of beta amyloid (Aβ) aggregates that are considered one of the causes of the pathology. On these bases, hundreds of molecules have been tested, as possible AD therapeutics active to disaggregate Aβ fibrils or prevent their formation.[1-4] Also, Aβ has been under consideration to develop biomarkers for the early diagnosis and/or the appropriate monitoring of AD. Specific patterns of Aβ(1-40) and Aβ(1-42) concentrations in human blood and cerebrospinal fluid (CSF) are considered part of the laboratory AD diagnostic criteria.[5] However, due to the invasiveness and the struggle to obtain CSF samples, there is a great interest to develop AD biomarkers to be detected in the blood with high sensitivity and accuracy.[6, 7]

Among the molecules tested to target Aβ aggregation, peptides have been extensively used as they have suitable properties to interact with the peptide-peptide interface characterized by large, featureless surfaces [8-11] and high structural plasticity.[12] The first peptides to be tested corresponded to the central fragment of Aβ(1-42) found to exert β-sheet breaker activity.[13-16] Since then, many other peptides have been experimented: corresponding to different segments of Aβ(1-42) sequence, or including non-natural amino acids, or characterized by retro-inverse sequences.[17-23] Many of these are in an advanced experimental phase and are considered good candidates for clinical applications.[24-29]

More recently, the hypothesis has spread within the scientific community that immunotherapy targeting Aβ peptide has great potential for treating or preventing AD. Accordingly, many monoclonal antibodies against Aβ(1-42) have been developed. They vary by immunoglobulin G (IgG) class and differ considerably concerning the epitopes they target and the state of Aβ - monomers, oligomers, protofibrils, and fibrils - that recognize. Aducanumab and BAN2401 target Aβ oligomers and amyloid fibrils, whereas all the others target Aβ monomers.[13] In particular, bapineuzumab and aducanumab are humanized monoclonal antibodies targeting the Aβ(1-42) N-terminus; ponezumab is directed against the C-terminus; solanezumab and crenezumab against the central region. Administration of exogenous antibodies has the advantages of ensuring consistent antibody titers and eventually stopping adverse events, even if it requires repeated administrations and suffers from the high production cost.[30]

In this context, part of my research activity focused on developing a research strategy to overcome these limitations. Starting from the crystal structure Aβ-antibody binding site, we

have designed short peptide sequences with the intend of substituting the parent antibody in therapeutic and diagnostic applications.[31] Short peptides offer the advantage of easy and reproducible synthesis, have high chemical stability, and low production costs; moreover, they can be optimized in their activity and selectivity by following the standard structure-activity relationship protocols.[32, 33]

Accordingly, part of my thesis reports the design, synthesis, structural analysis of new ligands of Aβ(1-42) designed on the model of the binding sites of different monoclonal antibodies. In particular, we selected solanezumab[34] and crenezumab[35] that bind ^{16}K-S^{26} and ^{13}H-D^{23} Aβ(1-42) segments and aducanumab[36] that targets the ^{3}E-E^{11} N-terminal fragment. The designed peptides were studied for their interaction with Aβ(1-42) using CD and NMR spectroscopies; their effect on the Aβ(1-42) aggregation was studied using atomic force microscopy.

2. Results

2.1. Peptide design

The crystallographic structures of several antibodies developed against Aβ(1-42) are available in the protein data bank on their own or cocrystallized with their epitope targets. Among those, we focused on solanezumab,[34] crenezumab[35], and aducanumab[36]. Solanezumab and crenezumab target the epitopes ^{16}KVLFFAEDVGS^{26} and ^{13}HHQKLVFFAEDV^{24}, including residues critical for Aβ aggregation and important for the β-sheet breaker function.[14] Aducanumab targets the ^{3}EFRHD^{7} epitope. Its clinical trial, previously interrupted because of poor results, has been recently resumed.[37]

2.1.1. Design of WAibH peptide

Analysis of solanezumab structure cocrystallized with ^{16}KVLFFAEDVGS^{26} Aβ(1-42) epitope (PDB ID: 4XXD)[34] shows that light and heavy chains of the antibody participate in the bindings site. ^{34}H and ^{96}W, whose aromatic rings are at about 7Å distance, establish important π-π stacking interactions with ^{19}F-F^{20} (**Figure 1**). The binding pocket architecture is very similar to that of crenezumab (PDB ID: 5VZY), including 7Å distant H and W aromatic rings.[35] Moreover, in this case, the binding is stabilized by hydrogen bonds involving crenezumab ^{52}S and ^{33}G (heavy chain) with Aβ(1-42) ^{22}E and ^{23}D. (**Figure 1C-D**).

Based on these observations, we designed a small library of peptide W-(X)n-H sequences (**Table 1**), where the spacer X is thought to mimic the hydrophobic nature of the antibody binding pocket and the 7Å distance between W and H aromatic rings. Accordingly, X

includes one or two Ala residues and the non-natural α-aminoisobutyric acid (Aib) residue; this, including an extra methyl, is rigid, highly hydrophobic, and validated for its propensity to bind Aβ(1-42) in anti-aggregating biological assays.[38]

Table 1: Peptide ligand designed from Aβ(1-42)/solanezumab and Aβ(1-42)/crenezumab binding sites. In the table is reported the energy of interaction with Aβ(1-42) as value of docking score and the percentage of poses (out of 100) with a root-mean-square deviation (RMSD) of backbone atoms position ≤ 3.

Ligand	***Docking score (kcal/mol)***	***% of poses with RMSD ≤ 3***
KLVFF	**-7.0**	**60%**
WAH	-4.6	48.7%
WAAH	-4.7	60%
WAibH	-5.7	66.7%
WAAibH	-4.5	85.7%
WAibAH	-6.0	30.8%
WAPH	-5.9	32%

The designed sequences were subjected to molecular docking calculation (AutoDock Vina) using as target the NMR structure of Aβ(1-42) in HFIP/water 50/50 v/v (PDB ID: 6SZF). The calculation was carried out by setting the grid box on the Aβ(1-42) antibody-epitope ^{15}QKLVFFA^{21}; the β-breaker peptide KLVFF was used as a positive control.[14] By analyzing the docking score values reported in **Table 1**, WAibAH and WAPH (-6.0 and -5.9 kcal/mol, respectively) appear the best candidates as Aβ(1-42) ligands. However, based on the highest number of reproducible poses (66.7% poses with RMSD ≤ 3 Å) we decided to synthesize WAibH for subsequent interaction studies.

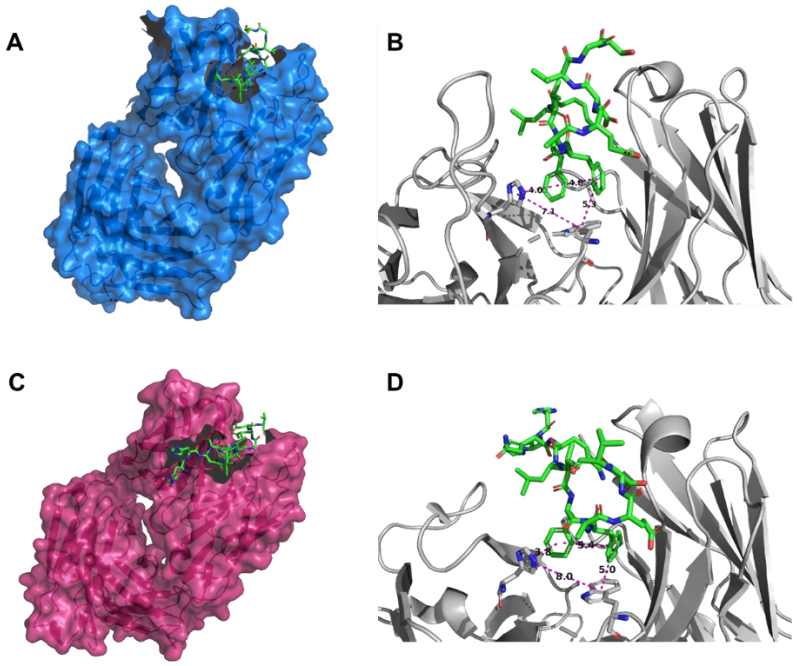

Figure 1. A) X-ray structure of solanezumab (blue surface) co-crystallized with the Aβ(1-42) epitope (green) (PDB ID: 4XXD). **B)** Zoom on the π-π stacking interactions between ^{19}F and ^{20}F of Aβ(1-42) (green) and ^{34}H and ^{96}W of solanezumab light chain (grey), in purple the distances between the aromatic rings. **C)** X-ray structure of crenezumab (pink surface) cocrystallized with the Aβ(1-42) epitope (green) (PDB ID: 5VZY) **D)** Zoom on the π-π stacking interactions between ^{19}F and ^{20}F of Aβ(1-42) (green) and ^{34}H and ^{96}W of crenezumab light chain (grey), in purple the distances between the aromatic rings.

2.1.2. Design of SYSTPGK peptide

The crystal structure of aducanumab cocrystallized with ^{3}EFRHD^{7} epitope (PDB ID: 6CO3)[36, 39] shows the epitope dunked in a "glove like" fitting binding pocket (**Figure 2)**. A careful observation of the binding site indicates H-bonds involving i) ^{92}Y and ^{93}S aducanumab light chain with ^{6}H and ^{4}F of Aβ(1-42) epitope; ii) ^{105}R heavy chain with ^{5}R Aβ(1-42) epitope. Moreover, an important salt bridge is observable between ^{65}K of the aducanumab heavy chain and ^{3}E of Aβ(1-42) epitope (**Figure 3**). **Table 2** reports the sequences designed to reproduce these interactions and subjected to molecular docking simulations by following the protocol previously described.

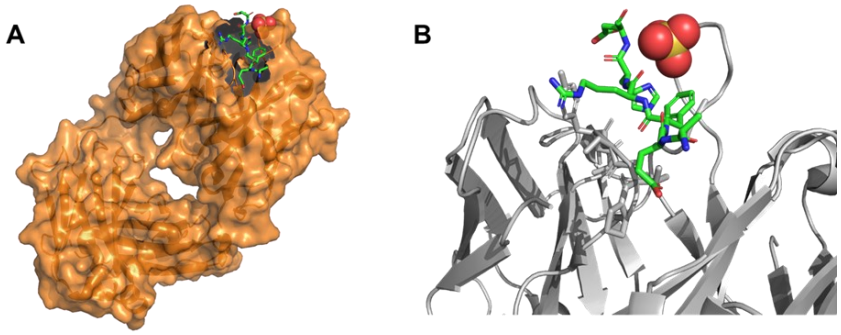

Figure 2. A) X-ray structure of aducanumab (orange surface) cocrystallized with the Aβ(1-42) epitope (green) (PDB ID: 6CO3). **B)** Zoom on the residues of aducanumab light and heavy chain (in grey) that interact Aβ(1-42) epitope ^{3}EFRHD^{7} (green).

Analysis of docking score and the number of binding poses RMSD ≤ 3 indicates that SYSTPGK sequence is the most promising candidate for Aβ(1-42) binding. It shows the lowest docking score value and the highest number of binding poses with RMSD ≤ 3; moreover, it includes lysine as C-terminal residue, characterized in the sidechain, by chemical moieties suitable for salt bridge interactions, analogously to what was observed for the aducanumab-Aβ(1-42) epitope binding pocket.

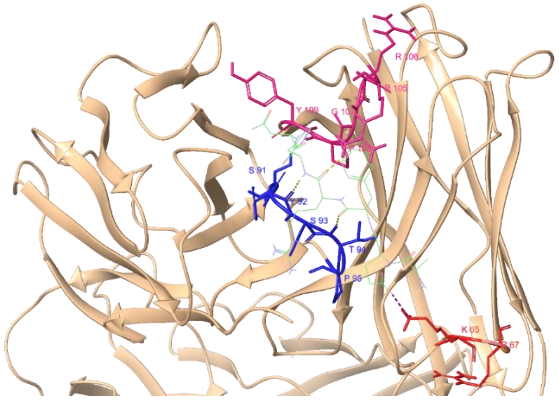

Figure 3: Binding pocket of aducanumab (yellow ribbon) in complex with amyloid ^{3}EFRHD^{7} epitope (light green) (PDB ID: 6CO3). The highlighted residues were considered for the building of the library containing peptides designed from the aducanumab.

Table 2: Peptide ligand designed from Aβ(1-42)/aducanumab binding site. In the table is reported the energy of interaction with Aβ(1-42) as value of docking score and the percentage of poses (out of 100) with a root-mean-square deviation (RMSD) of backbone atoms position ≤ 3.

Ligand	*Docking score (kcal/mol)*	*% of poses with RMSD ≤ 3*
KLVFF	**-7.0**	**60%**
SYSTPGK	-6.9	57.4%
YPGRGY	-5.5	62%
YPGRR	-6.8	35.2%
SYSTPR	-5.4	40.2%

2.2. Structure determination

WAibH and SYSTPGK peptides were obtained by following the standard solid phase peptide synthesis (SPPS) procedures.[40]

NMR conformational analysis of WAibH and SYSTPGK was carried out in HFIP/water 50/50 v/v, the same solvent mixture employed for Aβ(1-42). Homonuclear 2D TOCSY and NOESY and heteronuclear ^{1}H-^{13}C-HSQC experiments were recorded on Bruker DRX-600 spectrometer to allow for the proton chemical shift assignment, according to the procedure developed by Wuthrich.[41] The spectra were analyzed using SPARKY software.[42] ^{1}H and ^{13}C chemical shifts are reported in **Tables 3** and **4**.

Table 3. ^{1}H and ^{13}C chemical shifts of WAibH peptide in HFIP/water 50/50 v/v.

	Proton Chemical shift (ppm)				**Carbon – Proton Chemical Shift (ppm)**		
Residue	**HN**	**Hα**	**Hβ**	**H-Others**	**CHα**	**CHβ**	**CH-Others**
Trp[1]	7.20	4.22	Hβ2: 3.33 Hβ3: 3.29	Hδ1: 7.23 Hε3: 7.61 Hζ3: 7.11 Hη2: 7.19 Hζ2: 7.42 NH: 9.54	54.91	27.92	Cδ1: 126.10 Cε3: 119.14 Cζ3: 120.70 Cη2: 123.36 Cζ2: 113.10
Aib[2]	7.06	/	Qβ1: 1.12 Qβ2: 1.09		/	Cβ1: 23.61 Cβ2: 25.60	
His[3]	7.35	4.45	Hβ2: 3.22 Hβ3: 2.99	Hδ2: 7.12 Hε1: 8.44 HN: 8.37	54.16	27.82	Cδ2: 117.89 Cε1: 134.08

Table 4. ^{1}H and ^{13}C chemical shifts of of SYSTPGK peptide in HFIP/water 50/50 v/v.

	Proton Chemical shift (ppm)				Carbon – Proton Chemical Shift (ppm)		
Residue	**HN**	**Hα**	**Hβ**	**H-Others**	**CHα**	**CHβ**	**CH-Others**
Ser[1]	8.11	/	Qβ: 3.85		/	60.40	
Tyr[2]	7.96	4.51	Hβ2: 3.00 Hβ3: 2.88	Qδ: 7.03 Qε: 6.73	55.84	35.86	Cδ: 130.46 Cε: 115.30
Ser[3]	7.97	4.393	Qβ: 3.74		55.59	61.12	
Thr[4]	7.75	4.552	4.10	Qγ2: 1.11	56.47	66.84	Cγ2: 18.44
Pro[5]	/	4.273	Hβ2: 2.16 Hβ3: 1.82	Hγ2: 1.96 Hγ3: 1.87 Hδ2: 3.65 Hδ3: 3.55	61.02	28.82	Cγ: 24.28 Cδ: 48.07
Gly[6]	8.00	Hα2: 3.94 Hα3: 3.68			42.35		
Lys[7]	7.50	4.15	Hβ2: 1.74 Hβ3: 1.60	Qγ: 1.27 Qδ: 1.57 Qε: 2.88	54.56	31.24	Cγ: 21.76 Cδ: 26.22 Cε: 39.60

Analysis of NOE data in WAibH NOESY spectrum indicates the absence of sequential and medium-range correlations diagnostic of regular secondary structure. Regarding SYSTPGK, analysis of the NOESY spectrum reveals the presence of consecutive N,N(*i*,*i*+1), α,N(*i*,*i*+1) and α,β(*i*,*i*+1) connectivities (**Figure 4B**). These, translated in interprotonic distances, have been used as restraints for NMR structure calculation using CYANA software.[43] **Figure 4A** shows the SYSTPGK NMR structure, out of the 50 calculated, having the lowest target function score. Analysis of the backbone dihedral angles using PROMOTIF[44] indicates a bend structure encompassing the residues ^{3}S-P^{5}.

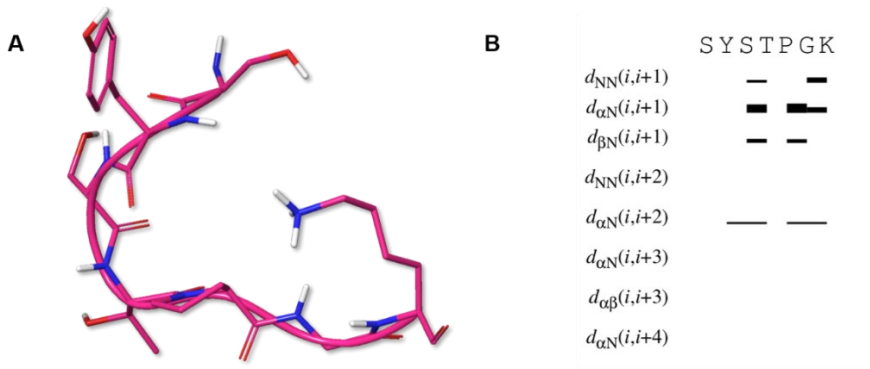

Figure 4. A) Low energy NMR model calculated for SYSTPGK peptide. The calculation was carried out using the standard CYANA protocol of simulated annealing in torsion angle space. **B**) Sequential and medium-range NOEs used to calculate the SYSTPGK structure ensemble.

2.3. Interaction studies

2.3.1. CD interaction studies

The study of the interaction of WAibH and SYSTPGK with Aβ(1-42) was performed by CD and NMR spectroscopies in HFIP/water 50/50 v/v, to be consistent with the system previously employed for the conformational analysis of Aβ(1-42).

Figure 5A shows CD spectra of Aβ(1-42) in HFIP/water 50/50 v/v ratio, in the presence of increasing amounts of WAibH (1:0; 1:1; 1:5; 1:10). The CD curves are almost identical until to reach Aβ(1-42)/WAibH 1:5 molar ratio. A slight change in the CD curve, diagnostic of a slight change in the Aβ(1-42) conformation, is evident at Aβ(1-42)/WAibH 1:10 molar ratio.[45]

Figure 5B shows CD spectra of Aβ(1-42) in HFIP/water 50/50 v/v ratio, in the presence of increasing amounts of SYSTPGK (1:0; 1:2.5; 1:5). As shown, the addition of SYSTPGK in 1:5 molar ratio induces a conformational perturbation that can be quantitatively estimated as a 100% to 71% decrease in α-helical structure (DICHROWEB[45] using the CONTIN algorithm).

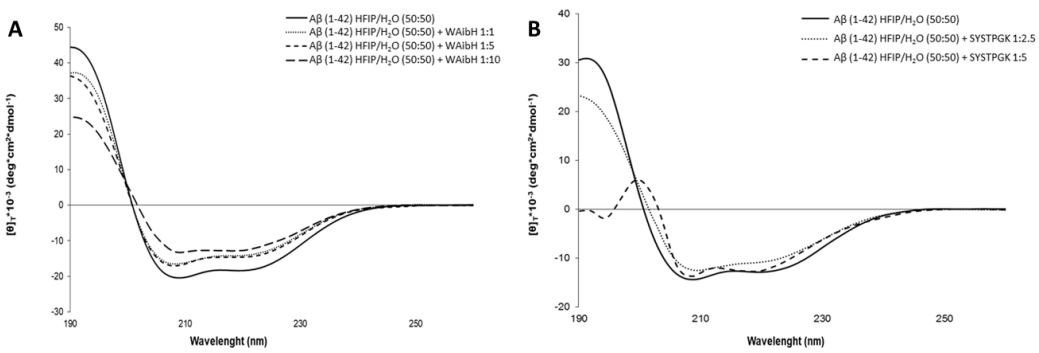

Figure 5. CD spectra of Aβ(1-42) in HFIP/water 50/50 v/v **A)** in the presence of increasing amounts of WAibH (1:1; 1:5; 1:10) and **B)** in the presence of increasing amounts of SYSTPGK (1:2.5; 1:5).

2.3.2. NMR interaction studies

2.3.2.1. STD experiments

The ^{15}N enriched Aβ(1-42) was produced by gene expression following the procedures previously described.[46, 47]

Interactions of WAibH and SYSTPGK peptides with Aβ(1-42), was studied using NMR saturation transfer difference (STD) experiments. **Figure 6** shows the STD NMR spectra acquired on Aβ(1-42)/WAibH sample in a 1:50 molar ratio. Analysis of STD effects indicates an extended Aβ(1-42)/WAibH interaction, with significant participation of ^{2}Aib methyl protons (δH= 0.96-1.05 ppm) and ^{1}W indolyl ring protons (the ζ2 δH =7.46 ppm), showing 7% and 3% STD effects (**Figure 6**).

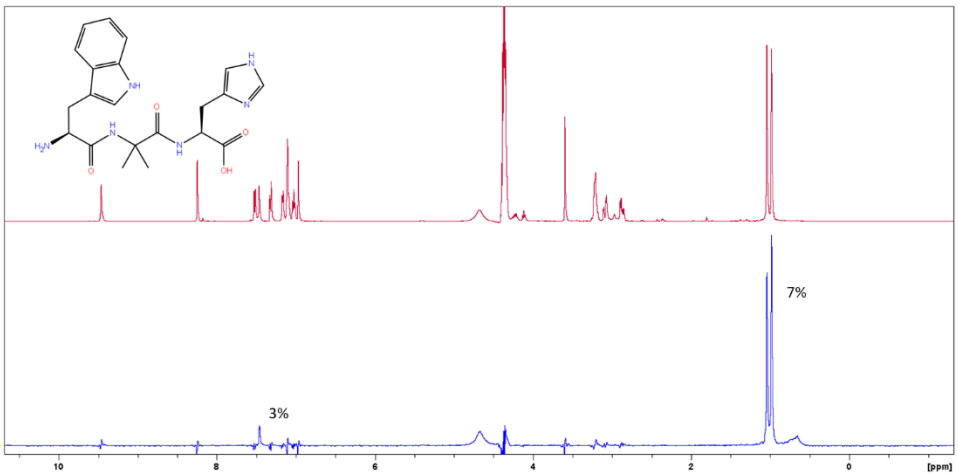

Figure 6. STD-NMR spectra of Aβ(1-42)/WAibH, 1:50 M ratio. Red shows the off-resonance spectrum and blue shows the STD spectrum.

Concerning SYSTPGK (**Figure 7**), STD experiments indicate the most significant effects for ^{4}T methyl protons (δH 1.09 ppm), with a 5% decrease in the signal intensity. Other STD

effects involve the δ protons of ^{5}P (δH = 3.55 ppm) and the γ and δ protons of ^{7}K (δH = 1.27 and 1.57 ppm).

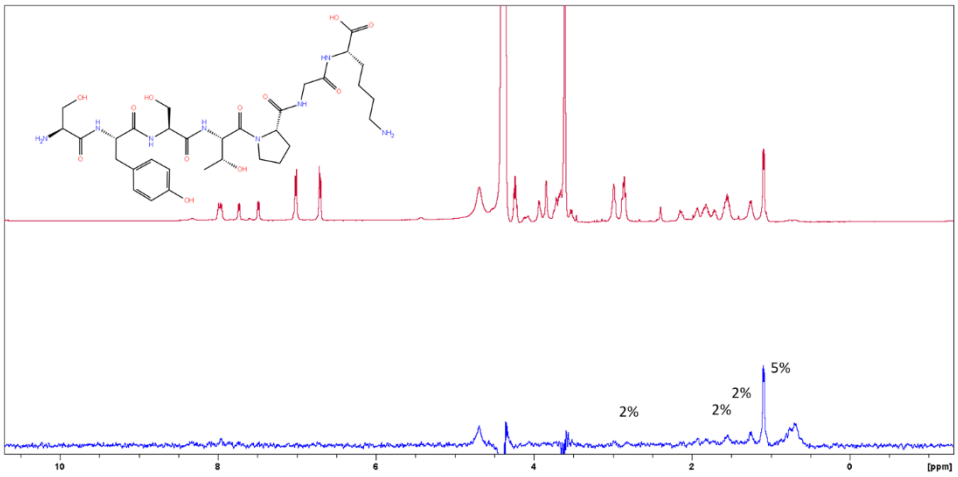

Figure 7. STD-NMR spectra of Aβ(1-42)/SYSTPGK, 1:10 M ratio. Red shows the off-resonance spectrum, and blue shows the STD spectrum.

2.3.2.2. Chemical Shift Mapping

Interaction of WAibH and SYSTPGK with Aβ(1-42) in HFIP/water 50/50 v/v was studied by chemical shift mapping experiments. The chemical shift assignment of all ^{1}H and ^{15}N signals was preliminarily carried out by analyzing ^{1}H-^{15}N-HSQC spectra of ^{15}N labeled Aβ(1-42) (SPARKY software),[48] supported by the data derived from the previous analysis of the 2D homonuclear TOCSY and NOESY spectra (*vide infra*).

Then ^{1}H-^{15}N-HSQC spectra of ^{15}N labeled Aβ(1-42) free and including increasing concentrations of ligands to reach ^{15}N Aβ(1-42)/WAibH 1:50 molar ratio, were acquired and analyzed.[49] Based on the ^{1}H and ^{15}N chemical assignment, the chemical shift perturbations (CSPs) were calculated as follows:

$$\Delta\delta_{NH}(ppm) = \sqrt{(\Delta\delta\,^{1}H + (0.154 * \Delta\delta\,^{15}N)^2}$$

As reported in **Figure 8A**, CSPs are significant for residues ^{5}R-E^{22}. In particular, the most pronounced CSPs are relative to ^{5}R and ^{10}Y backbone NHs. These were used for a quantitative estimation to calculate the K_D (dissociation constant) of the interaction according to the equation below:[50]

$$\Delta\delta_{obs} = \Delta\delta_{max}\frac{([P]_0 + [L]_0 + K_D) - \sqrt{([P]_0 + [L]_0 + K_D) - 4\,[P]_0[L]_0}}{2[P]_0}$$

[P] = protein concentration, [L] = concentration of ligand, $\Delta\delta_{max}$ = the greatest observed chemical shift change.

According to this calculation, K_D of Aβ(1-42)/WAibH interaction is 5.74 mM (**Figure 8B**).

By following an analogous procedure, we analyzed the binding of SYSTPGK peptide with Aβ(1-42), having as the final titration point ^{15}N Aβ(1-42)/ SYSTPGK 1:10 molar ratio. Analysis of CSPs indicates chemical sift perturbation mainly interesting N terminal Aβ(1-42) sequence (**Figure 8C**). Quantitative estimation of CSPs related to the ^{15}N Aβ(1-42)/SYSTPGK ratios indicates a K_D of 0.650 mM, 10-fold lower than Aβ(1-42)/WAibH K_D.

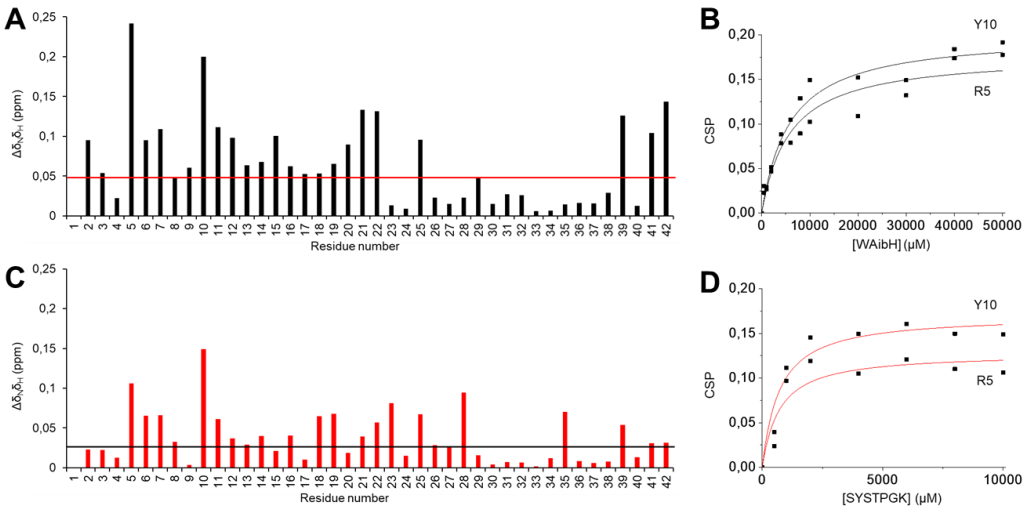

Figure 8. Aβ(1-42) and ligands interaction. **A)** Amide chemical shift perturbation of Aβ(1-42) by addition of WAibH (1:50), with the red line showing the average of the shifts. **B)** CSPs of the most perturbed chemical shift residues (^{5}R, ^{10}Y) as a function of WAibH concentration. **C)** Amide chemical shift perturbation of Aβ(1-42) by addition of SYSTPGK (1:10), with the black line showing the shifts' average. **D)** CSPs of the most perturbed Aβ(1-42) chemical shift residues (^{5}R, ^{10}Y) as a function of SYSTPGK concentration.

2.4. Model building by molecular docking

2.4.1. Molecular docking

To build a pseudo-pharmacophore model of WAibH and SYSTPGK ligand peptides in their interaction with Aβ(1-42), we repeated molecular docking calculations taking into account the results of NMR interaction studies. **Figure 9** shows structural models of WAibH and SYSTPGK docked on Aβ(1-42) NMR structure in HFIP/water 50/50 v/v (PDB ID: 6SZF). WAibH structure resulting from the previous *in silico* calculations was docked against Aβ(1-42) setting as restraints short distances from ^{5}R and ^{10}Y residues according to chemical shift mapping experiments (**Figure 8A**).

Figure 9A shows WAibH in its most favorable binding pose, characterized by a docking score (-5.7 kcal/mol) similar to the one calculated setting the grid on ^{16}KLVFF^{20} moiety

(**Table 1**). In particular, the ^{1}W indole moiety of WAibH forms two π-π stacking interactions with the ^{10}Y phenyl moiety of Aβ(1-42); the ^{3}H carboxyl moiety of WAibH sets a salt bridge and a hydrogen bond with ^{5}R side chain of Aβ(1-42) (**Figure 9B**). Other residues involved in the binding are ^{7}D (H-bond with the amino terminus of WAibH ^{1}W), ^{18}V (H-bond with the imidazole side chain of WAibH ^{3}H), and ^{11}E (hydrophobic interactions with WAibH backbone).

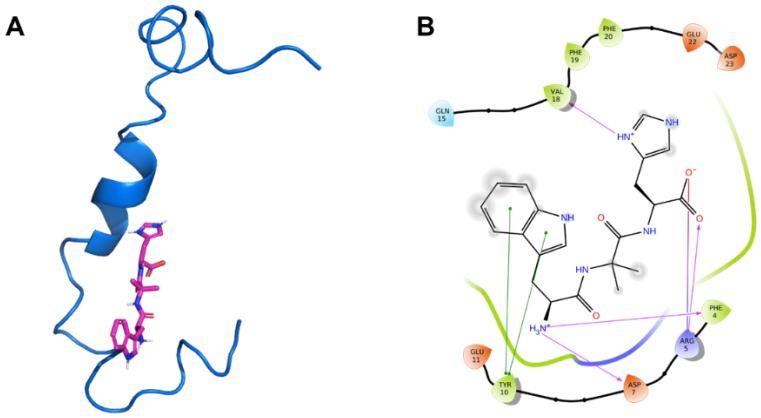

Figure 9. A) Binding pose of WAibH (magenta) with Aβ(1-42) (blue ribbon) (PDB ID: 6SZF) obtained from molecular docking calculations. **B)** 2D Ligand interaction diagram that shows the salt bridges (pink arrows) and the π-π stackings (green arrows) in the binding pose obtained from docking calculations.

Regarding SYSTPGK, molecular docking calculations were repeated, setting as restraints the short distances with ^{5}R and ^{10}Y Aβ(1-42) residues (**Figure 8C**). NMR structure of SYSTPGK previously calculated (**Figure 4A**) was used as a starting ligand structure. **Figure 10A** shows SYSTPGK in its most favorable pose, which presents a docking score (-6.8 kcal/mol) (**Table 2**). Interaction of SYSTPGK with Aβ(1-42) involves the π-cation stacking between ^{2}Y and Aβ(1-42) ^{5}R; the hydrophobic interaction between ^{1}S of SYSTPGK and Aβ(1-42) ^{10}Y (**Figure 10B**). Additional interactions involve ^{1}D and ^{3}E, establishing H-bonds with SYSTPGK ^{7}K; ^{7}D and ^{15}Q establishing H-bonds with ^{1}S, ^{11}E establishing hydrophobic interaction with SYSTPGK backbone.

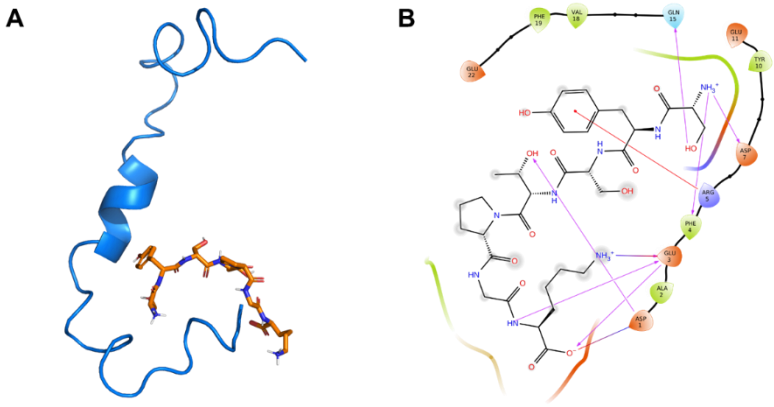

Figure 10. A) Binding pose of SYSTPGK (orange) with Aβ(1-42) (blue ribbon) (PDB ID: 6SZF) obtained from molecular docking calculations. **B)** 2D Ligand interaction diagram that shows the salt bridges (pink arrows) and the π-cation stackings (red arrows) in the binding pose obtained from docking calculations.

2.5. AFM Microscopy

The aggregation response of Aβ(1-42) in the absence and in the presence of WAibH and SYSTPGK ligands aged for 192 hours in phosphate buffer at room temperature was investigated at the nanoscale by means of AFM imaging. The AFM morphologies of Aβ(1-42) in the absence and in the presence of WAibH and SYSTPGK ligands are reported in **Figure 11A**, **B** and **C** respectively. All the images are 10 μm × 10 μm in lateral size. Black-to-white colour scale, spanning between 0 and 1 nm, is used to show the height corrugation, with black and white being the lowest (0 nm) and highest (≥ 1nm) point in the maps, respectively. Independently from the sampled area, a clear morphological difference is always evident among the three investigated samples. Indeed, while Aβ(1-42) (**Figure 11A**) exhibits a full variety of morphological structures, such as mature fibrils (MF), bundles of fibrils (BF), protofibril (PF), and small spherical aggregates (SA), MF and BF are totally absent in WAibH (**Figure 11B**) and SYSTPGK (**Figure 11C**), with only the latter, occasionally showing some bead assembled PF. On the other hand, they all show a carpet of SA, 2-3 nm in height, as well as occasional SA clusters or aggregates, measuring, on average, hundreds of nm in diameter and only few nm in height.

The measurement of MF characteristic size and height has been carried out only by studying the sample Aβ(1-42) (**Figure 11A**), resulting in a range of 20–30 nm in diameter and 2–3 nm in height. Moreover, some of those fibrils appear twisted and coiled in BF with an almost incoherent orientation. These observations are in full agreement with the existing literature on fibrillization in Aβ(1-42). Such a result strongly indicates that the used "incubation" time (192h) is long enough, in general, to induce the fibrillization process at

room temperature, further reinforcing the hypothesis of fibrillization inhibition both in Aβ(1-42) in the presence of WAibH and SYSTPGK, where neither MF nor a significative number of PF have been observed among all the imaged areas.

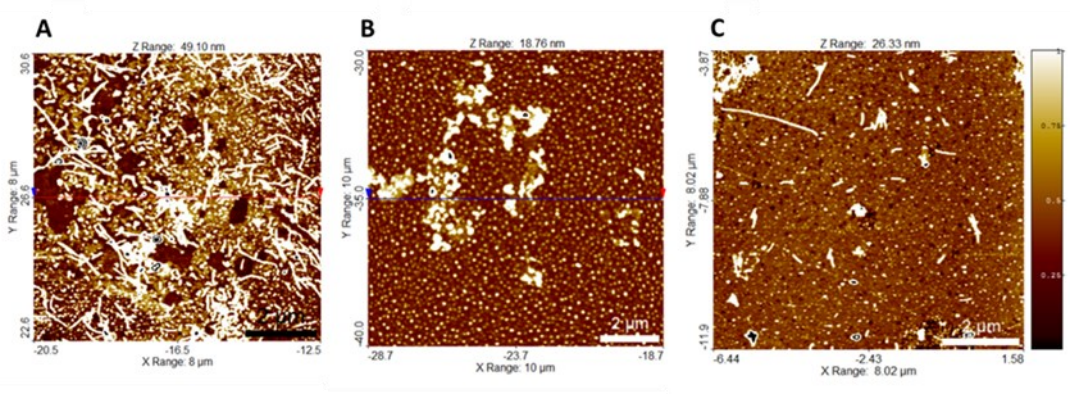

Figure 11. AFM morphologies of Aβ(1-42) in the absence **(A)** and in the presence of WAibH **(B)** and SYSTPGK **(C)** ligands.

Here, we want to underline that the measurement of the lateral size of the investigated objects can be affected by a systematic error, due to the finite size of the AFM probe (the used tips had a nominal radius of 10 nm). Indeed, whenever the size of the tip becomes comparable to or bigger than the grain size, the measure of the lateral size of the grain is overestimated. For this reason, a direct AFM measure of the height, rather than the lateral size, is considered more reliable.

In the following, we present a systematic procedure of grain analysis performed on the acquired AFM images and aimed to select individually different families of morphological structures, distinguishing the mature fibrils (MF) from the other structures and extracting their characteristic size.

First, the relevant structures have been identified to be separated from the background by setting a threshold condition on their minimum height. Subsequently, threshold filters based on the object shape (length and/or roundness) have been employed to discriminate between different families of structures (for instance: (1) SA are almost round, whereas MF elongates mainly in one direction (2) MF are certainly longer than SA - see Material and methods section). By doing so, MF (and their aggregates) can be individually selected, counted, and measured. We applied this procedure on five images, 3 µm × 3 µm in lateral size, for each sample, acquired in various locations of the surface.

As an example, **Figure 12** shows the visual result of the grain analysis procedure, implemented on Aβ(1-42) in the same area as **Figure 11A**. In this case, we first fixed a

minimum threshold height of 0.5 nm (any object protruding more than 0.5 nm from the mica surface has been included in the analysis). Then, given the value "1" as the roundness of a perfect circle, we fixed a roundness reference value of 0.5 and a length reference value of 200 nm (in agreement with the typical size reported in the literature for PF).

Figure 12A identifies and highlights in blue, green, and red the structures with roundness higher than 0.5 and characteristic length of 0.5-50 nm (blue), 50-100nm (green), and 100-200nm (red). On the other hand, **Figure 12B** identifies and highlights in blue, green, and red the structures (MF) with roundness lower than 0.5, and characteristic length of 200-400 nm (blue), 400-800nm (green), and >800nm (red).

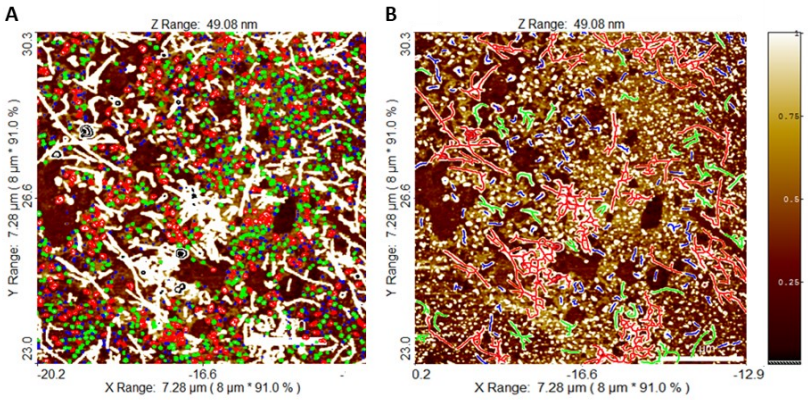

Figure 12. Qualitative results of the grain analysis of Aβ(1-42). On the left are reported the small spherical aggregates with length of 0.5-50 nm (blue), 50-100nm (green) and 100-200nm (red). On the right are reported the mature fibrils with length of 200-400 nm (blue), 400-800nm (green) and >800nm (red).

In addition to this, the total volume occupied in the image by MF, VMF, has been calculated, compared to the total volume occupied by the other structures, VOS, and used as an indicator of the degree of fibrillization (DoF), as DoF= VF/VOS. By doing so, samples with higher DoF, will correspond to the ones where the fibrillation is enhanced. Again, we underline that, since those volume estimates can be affected by the geometric properties of the used tip, this comparison has been done among images acquired with the same AFM probe. **Table 5** reports the results in terms of VMF, VOS, DoF, MF counts, OS counts and their % ratio.

Table 5. Quantitative analysis of the structures

	Aβ(1-42)	WAibH	SYSTPGK
V_{OS} **(106 nm^3)**	2.59E+06	1.30E+06	1.22E+06
V_{FM} **(106 nm^3)**	2.96E+07	4.08E+06	7.40E+06
DoF	0.11	0.03	0.06
S Counts	1404	2329	2563
F Counts	172	126	156
N% (F Counts)/(S Counts)	12.2	5.4	6.0

3. Discussion

Immunotherapy has been receiving increasing interest as an innovative approach to treat Alzheimer's disease. Many monoclonal antibodies against Aβ(1-42) have been developed. Solanezumab and crenezumab target the central Aβ(1-42) region; aducanumab target Aβ-oligomers on the Aβ(1-42) N-terminal portion.[13] The crystal structures of solanezumab, crenezumab, and aducanumab cocrystallized with the respective epitopes are deposited in the PDB database (PDBID: 4XXD, 5VZY and 6CO3 respectively). A small library of peptides was designed based on the structural features of the single antibody-Aβ(1-42) binding site, starting from these crystal structures. Among the peptide sequences screened using molecular docking calculations, WAibH and SYSTPGK were identified as the best Aβ(1-42) ligand candidates. They were synthesized and studied by CD and NMR spectroscopies for their ability to interact with Aβ(1-42). NMR experiments show that WAibH binds Aβ(1-42); this interaction does not affect the Aβ(1-42) conformation as demonstrated by CD spectra, which remain almost unchanged upon increasing WAibH concentration. On the contrary, the interaction of SYSTPGK with Aβ(1-42) induces a decrease in α-helical structure.

Based on STD and chemical shift mapping experiments, the binding mode Aβ(1-42)/WAibH and Aβ(1-42)/SYSTPGK was characterized. STD experiments indicate that the methyl moiety of ^{2}Aib and ^{1}W indolyl rings has a major role in Aβ(1-42)/WAibH interaction. On the other side, according to chemical shift mapping data, the binding of WAibH to Aβ(1-42), (5.4 mM K_D constant), perturbs residues belonging to different parts of Aβ(1-42) sequence, with significant participation of the central Aβ(1-42) residues, in agreement with the computer modeling prediction.

^{4}T, ^{5}P, and ^{7}K of SYSTPGK peptide interact with Aβ(1-42) according to STD data. Conversely, a network of NH chemical shift changes, mainly regarding the central and N-terminal Aβ(1-42) portion, confirm significant interaction with Aβ(1-42). The binding (650 μM K_D constant) involves the N-terminus, in agreement with the computer modeling prediction, but is also extended to the central part of the sequence.

It is noteworthy that WAibH and SYSTPGK can inhibit Aβ(1-42) aggregation, as shown by AFM microscopy. They inhibit the formation of Aβ(1-42) mature fibrils, with an effect that can be quantitatively estimated by a decrease of degree of fibrillization from 0.11 to 0.03 for WAibH and 0.06 for SYSTPGK.

Taken together, our data show that WAibH and SYSTPGK are endowed with an interesting ability to bind Aβ(1-42). Although characterized by a modest K_D binding constant, they represent a valuable starting point to design new peptides endowed with improved binding properties. Compared to their antibody parents, they can be easily synthesized using high reproducible and low-cost chemical synthesis; moreover, thanks to their minimal size, they may be suitable for nanoparticle functionalization in diagnostic applications.

4. Materials and Methods

4.1. Molecular docking

Molecular docking calculations were carried out with AutoDock 4.2[51] and AutoDock Vina[52]. Aβ(1-42) structure obtained from NMR spectra assignment in HFIP/water 50/50 v/v was set as receptor protein. Three grid boxes were used: one incorporating the Aβ(1-42) moieties corresponding to ^{15}QKLVFFA^{21} for the docking with the peptides designed from solanezumab and crenezumab, one including the residues ^{3}EFRHD^{7} for the docking with the peptides designed from aducanumab, and one having as center Aβ(1-42) residues ^{5}R and ^{10}Y for the calculations aimed to build the *in silico* model of the NMR interaction. The designed peptide ligands were built using the Python script *build_peptide.py* included in Maestro 11.8.012[53] run directory, which permitted to have the peptide 3D structure from a text file containing its one letter sequence. The non-natural amino acid Aib (α-amino isobutyric acid) was obtained adding an extra methyl group on Ala. Results were analysed according to lowest docking scores (kcal/mol), which indicate the binding poses with the most favourable interaction energies, and lowest values of RMSD, which represent the reproducibility of the poses. Poses with docking score < -4 kcal/mol and RMSD ≤ 3 were selected and evaluated. Molecular visualization was performed with Maestro and PyMOL[54].

4.2. Sample Preparation

4.2.1. ^{15}N Aβ(1-42) peptide production

^{15}N Aβ(1-42) peptide was obtained after transformation of *E.Coli* BL21(DE3)-pLysS cells with PetSac plasmid provided by the research group of Walsh.[46] To optimize expression levels, were used E. Coli, Ca^{2+}-competent (BL21(DE3)-pLysS) cells obtained by thermal shock and allowed to grow in agar plates containing the LB culture medium with ampicillin (50 mg/L). The individual colonies were taken from a stock solution, stored at a temperature of -80 °C, and added to 50 mL of preinoculum, where 50 µL of ampicillin (50 mg/L) was previously added. The preparation was left in a thermostatic incubator, under constant stirring, at a temperature of 37 °C for the overnight. The following day, 5 mL of the culture was transferred to 500 mL of LB medium added with 500 µL of ampicillin (50 mg/L). When cell density had reached an OD_{600} of 0.3 at 37 ° C, the medium was centrifuged and the pellet was resuspended in M9 medium.[47] When cell density reached a final OD_{600} of 0.6 at 37°C, isopropyl-thio-β-D-galactoside (IPTG), gene expression inducer, was added. The cells were collected after 4h of induction and centrifuged to remove the fraction constituted by the supernatant. Subsequently, the resulting pellet was thawed and sonicated three times in a solution containing: Tris/HCl pH 8.0 and EDTA, at a concentration of 10 mM and 1 mM respectively, for 5 minutes on ice (1/2 horn, 50% duty cycle). The sonicate was centrifuged for 10 minutes at 8000 rcf. The supernatant was removed, and the pellet was resuspended in a solution containing: 8 M urea, Tris/HCl pH 8.0 10 mM, EDTA 1 mM and sonicate as before. The resulting solution, containing Aβ(1-42) in the urea-soluble inclusion bodies, was diluted with a 10 mM Tris/HCl solution pH 8.0 and 1 mM EDTA. Subsequently, the solution was purified with a HiTrap® column, at a flow rate of 1 mL/min, using an AKTA purification system. The protein was eluted with an elution buffer (8 M urea, Tris/HCl pH 8.0 10 mM, 1 mM EDTA, 1 M NaCl). The eluted fraction was subsequently dialysed against Tris/HCl pH 8.0 10 mM and freeze-dried. The purity of the peptide was verified using the SDS-PAGE electrophoretic technique, electrophoresis on polyacrylamide gel (PAGE) in the presence of sodium dodecyl sulphate (SDS), using Coomassie Blue Staining. The SDS-PAGE electrophoresis of the previously sonicated cell pellet revealed that the majority of ^{15}N Aβ(1-42) was present in the band between 4 and 5 kDa. In order to support the peptide expression, the MALDI (Matrix-Assisted Laser Desorption / Ionization) mass spectrometry technique was used. The sample was previously dried and placed in a MALDI sample support consisting of a solution matrix. (4-hydroxy acid, α-cyanic cinnamic,

25 mM citric acid), which favours the crystallization of the compounds and allows an optimal analysis.

4.2.2. CD and NMR Sample preparation

^{15}N Aβ(1-42) has a very high tendency to form fibrils. To preserve the peptide in the monomeric form and avoid the formation of oligomeric and polymeric forms, before and during the experiments, ^{15}N Aβ(1-42) was subjected to a defibrillating treatment following the procedure described by Jao et al.[55] (The peptide was dissolved in trifluoroacetic acid (TFA) until complete solubilization of the powder sample and left in TFA for 3 h. Subsequently, the TFA was removed under nitrogen flow and water was added to the sample for freeze-drying. This procedure was adopted for CD and NMR analysis immediately before dissolution in the appropriate solvent

4.2.3. Peptides synthesis

WAibH and SYSTPGK, were manually synthesized using Fmoc/tBu solid-phase peptide synthesis (SPPS) following Merrifield strategy.[40] Amino acids Fmoc-protected were coupled using 1-hydroxybenzotriazole and O-(benzotriazol-1-yl)-1,1,3,3-tetramethyluroniu mhexa-fuorophosphate (four-fold excess) as coupling reagents, at the solution was added six-fold excess of N,N-diisopropylethylamine as scavenger. The complex peptide/resin (Wang resin) was cleaved and the side chain was deprotected using a solution of 90% trifluoroacetic acid (TFA), 5% water and 5% triisopropylsilane (TIS) for 3 h. After the cleavage step the functionalized resin was filtered using a cold solution of diethyl ether in order to precipitate the peptide. Finally, the peptide was purified by reversed phase chromatography (HPLC) using Phenomenex C18 column. The peptides were characterized on a Finningan LCQ Deca ion trap instrument equipped with an electrospray source (LCQ Deca Finnigan, San José. CA, USA). The samples were directly infused in the ESI source using a syringe pump at a flow rate of 5.0 mL/min. The data were analyzed using the Xcalibur software. The sample purity was >98%.

4.3. CD experiments

The CD spectra were obtained using a JASCO J-810 spectropolarimeter, with the aid of a 1 cm long quartz cell and working at a temperature of 25 °C. The CD spectra were obtained by an average of 4 scans, in a measuring range 260-190 nm, at a bandwidth of 1 nm and, at a scanning speed of 10 nm/min. Each spectrum was processed by subtracting the solvent spectrum. The analysis of the CD curves was performed using the SELCON3 and CONTINN algorithms of the online platform DICHROWEB[45, 56]. All CD spectra were

acquired with a concentration of Aβ(1-42) of 0.15 mM. The solvent system used, for both interaction studies, was HFIP/water. For the interaction of Aβ(1-42)/WAibH, increasing amount of ligand were added in order to obtain the following molar ratio: (1:0; 1:1; 1:5 and 1:10). For the interaction with SYSTPGK, a solution containing Aβ(1-42) (0.15 mM) was added of increasing amount of the ligand in order to obtain the following molar ratio: (1:0; 1:2,5 and 1:5).

4.4. NMR experiments

4.4.1. STD experiments

STD-NMR experiments were recorded at 25 °C on a Bruker Avance 600MHz spectrometer at a ^{1}H resonance frequency of 600 MHz equipped with a 5 mm triple resonance $^{1}H(^{13}C/^{15}N)$, z-axis pulsed-field gradient probe head. All STD experiments were performed in HFIP/water 50/50 v/v. We decided to acquire these experiments using the concentration of the last point of the titration, therefore Aβ(1-42) peptide concentration was 0.5 mM and the concentration of WAibH and SYSTPGK was 25 mM and 5 mM respectively. For each experiment in the frequency list (FQ2LIST), the on-resonance and off-resonance pulses were 403 and 50000 Hz, respectively. Briefly, two free induction decay (FID) data sets were collected in an interleaved manner to minimize temporal fluctuations with Aβ(1-42) irradiation frequency set on-resonance (−0.5 ppm) and off-re-sonance (40 ppm) (sw = 6000 Hz, 16 steady-state scans, transients, 4k complex points, d1 = 3 s). Protein saturation was obtained using a train of individual 50 ms long and frequency selective Gaussian radio frequency (rf) pulses separated by an inter-pulse delay of 1ms. The FID acquired with off-resonance irradiation generated the reference spectrum (I_{off}), whereas the difference FID (off-resonance, on-resonance) yielded the STD spectrum (ISTD = I_{off}-I_{on}). Spectra were processed with an exponential apodization function (1 Hz line broadening) and zero-filling to 8k complex points before Fourier transformation and baseline correction with a third-order Bernstein polynomial fit. The STD measurements were performed in duplicate, and all data were processed and analysed using TopSpin software (Bruker v 3.5).

4.4.2. Chemical shift mapping experiments

NMR spectra were acquired on a Bruker DRX-600 spectrometer equipped with cryo-probe. ^{1}H-^{15}N-HSQC spectra[57] were transformed and visualized in Topspin (Bruker Biospin) and analyzed using SPARKY software[48] For the NMR analysis, ^{15}N Aβ(1-42) peptide in a 0.5 mM concentration was solubilized in an HFIP/water solution in a 50/50 v/v

ratio. All NMR samples contained 10% (v/v) D_2O, and 0.02% (w/v) sodium azide (NaN_3) as preservative.

For the interaction studies with WAibH, solutions of 0.5 mM ^{15}N Aβ(1-42) were prepared in duplicate. To one solution 25 mM WAibH was added. Using the two solutions different molar ratios of ^{15}N Aβ(1-42)/WAibH (1:0; 1:0.25; 1:0.5; 1:1; 1:2; 1:3; 1:4; 1:5; 1:6; 1:20; 1:30; 1:40 and 1:50) was obtained. For the interaction with SYSTPGK, solutions of 0.5 mM ^{15}N Aβ(1-42) were prepared in duplicate. To one solution 5 mM of SYSTPGK was added. As done before, using the two solutions, different molar ratios of ^{15}N Aβ(1-42)/SYSTPGK (1:0; 1:0.5; 1:1; 1:2; 1:6; 1:8 and 1:10) were obtained.

In order to determine protein-ligands binding affinities, dissociation constant (K_D) were calculated analysing the ^{15}N-^{1}H-HSQC spectra of ^{15}N Aβ(1-42) acquired for each titration point. The software used for the calculation of K_D was OriginPro 2019. (OriginPro, Version 2019. OriginLab Corporation, Northampton, MA, USA)

4.5. AFM Microscopy

The Aβ(1-42) preparations were dissolved in 10 mM phosphate buffer (pH = 7.4) until a concentration of 100mM and divided in three equal aliquots. One was used as the control sample while others were mixed with SYSTPGK and WAibH peptides keeping 1:20, Aβ(1-42)/peptides, molar ratio. All three aliquots were incubated at 37°C for 192 hours, a time long enough to assure the formation of mature fibrils in Aβ(1-42) control sample.

AFM samples were prepared by dropping 10 μL of solution onto a freshly cleaved mica (Ted Pella, Inc.) surface. After a waiting time of 5 minutes to allow the adhesion of most of the aggregates to the surface, the samples were rinsed twice the with bi-distilled water, dried with ultra-pure nitrogen and transferred to the AFM microscope for analysis.

AFM measurements were performed with a JPK Nanowizard 3 system operating in tapping mode (Alternate Contact) in dry air. The temperature was kept at 22 °C with a variation less than 0.3°C/h. Aβ(1-42) and the two peptide mixtures were scanned with the same silicon nitride cantilever (LTESP probes, Bruker), having a resonant frequency of 290 KHz and a nominal radius of curvature of 10-30 nm. The radius of curvature was measured at the end of experiments and it was found to be of about 50 nm, mainly due to contamination. To scan gently with a low action force the scan rate was set at 0.5 Hz and the amplitude set-point as high as possible, to achieve an equal forth and back fast axis scan trace. Images of areas ranging from 3 x 3 μm to 10 x 10 μm were collected with digital resolution of 512 x 512 pixels. The images were subjected to a standard background plane correction and removal of scan lines-streaks. Measurements and distribution of Aβ

aggregates dimensions were evaluated by using the grain analysis module of SPIP_Iamage Metrology and Origin Data analysis software.

References

[1] Lorenzi ED, Giorgetti S, Grossi S, Merlini G, Caccialanza G, Bellotti VJCmc. Pharmaceutical strategies against amyloidosis: old and new drugs in targeting a “protein misfolding disease”. 2004;11:1065-84.

[2] Soto C, Estrada LJAsD. Amyloid inhibitors and β-sheet breakers. 2005:351-64.

[3] Arkin MR, Wells JAJNrDd. Small-molecule inhibitors of protein–protein interactions: progressing towards the dream. 2004;3:301-17.

[4] Mason JM, Kokkoni N, Stott K, Doig AJJCoisb. Design strategies for anti-amyloid agents. 2003;13:526-32.

[5] Anoop A, Singh PK, Jacob RS, Maji SKJIjoAsd. CSF biomarkers for Alzheimer's disease diagnosis. 2010;2010.

[6] Baldacci F, Lista S, O’Bryant SE, Ceravolo R, Toschi N, Hampel H, et al. Blood-based biomarker screening with agnostic biological definitions for an accurate diagnosis within the dimensional spectrum of neurodegenerative diseases. Biomarkers for Alzheimer’s Disease Drug Development: Springer; 2018. p. 139-55.

[7] Hampel H, O’Bryant SE, Molinuevo JL, Zetterberg H, Masters CL, Lista S, et al. Blood-based biomarkers for Alzheimer disease: mapping the road to the clinic. Nature Reviews Neurology. 2018;14:639-52.

[8] Tanaka F, Shibata K, Monobe Y, Akagi K-i, Masuda YJB, Chemistry M. Design and synthesis of β-strand-fixed peptides inhibiting aggregation of amyloid β-protein. 2020;28:115676.

[9] Yao P, Zhang J, You S, Qi W, Su R, He ZJJoMCB. Ferrocene-modified peptides as inhibitors against insulin amyloid aggregation based on molecular simulation. 2020;8:3076-86.

[10] Mitra A, Sarkar NJAoB, Biophysics. Sequence and structure-based peptides as potent amyloid inhibitors: A review. 2020:108614.

[11] Spanopoulou A, Heidrich L, Chen HR, Frost C, Hrle D, Malideli E, et al. Designed macrocyclic peptides as nanomolar amyloid inhibitors based on minimal recognition elements. 2018;130:14711-6.

[12] Ribarič SJM. Peptides as potential therapeutics for Alzheimer’s disease. 2018;23:283.

[13] van Dyck CHJBp. Anti-amyloid-β monoclonal antibodies for Alzheimer’s disease: pitfalls and promise. 2018;83:311-9.

[14] Francioso A, Punzi P, Boffi A, Lori C, Martire S, Giordano C, et al. β-sheet interfering molecules acting against β-amyloid aggregation and fibrillogenesis. 2015;23:1671-83.

[15] Kokkoni N, Stott K, Amijee H, Mason JM, Doig AJJB. N-Methylated peptide inhibitors of β-amyloid aggregation and toxicity. Optimization of the inhibitor structure. 2006;45:9906-18.

[16] Amijee H, Bate C, Williams A, Virdee J, Jeggo R, Spanswick D, et al. The N-methylated peptide SEN304 powerfully inhibits Aβ (1–42) toxicity by perturbing oligomer formation. 2012;51:8338-52.

[17] Jiang N, Leithold LH, Post J, Ziehm T, Mauler J, Gremer L, et al. Preclinical pharmacokinetic studies of the tritium labelled D-enantiomeric peptide D3 developed for the treatment of Alzheimer s disease. 2015;10:e0128553.

[18] Handattu SP, Garber DW, Monroe CE, van Groen T, Kadish I, Nayyar G, et al. Oral apolipoprotein AI mimetic peptide improves cognitive function and reduces amyloid burden in a mouse model of Alzheimer's disease. 2009;34:525-34.

[19] Frydman-Marom A, Levin A, Farfara D, Benromano T, Scherzer-Attali R, Peled S, et al. Orally administrated cinnamon extract reduces β-amyloid oligomerization and corrects cognitive impairment in Alzheimer's disease animal models. 2011;6:e16564.

[20] Taylor M, Moore S, Mayes J, Parkin E, Beeg M, Canovi M, et al. Development of a proteolytically stable retro-inverso peptide inhibitor of β-amyloid oligomerization as a potential novel treatment for Alzheimer’s disease. 2010;49:3261-72.

[21] Hisatsune T, Kaneko J, Kurashige H, Cao Y, Satsu H, Totsuka M, et al. Effect of anserine/carnosine supplementation on verbal episodic memory in elderly people. 2016;50:149-59.

[22] Parthsarathy V, McClean PL, Hölscher C, Taylor M, Tinker C, Jones G, et al. A novel retro-inverso peptide inhibitor reduces amyloid deposition, oxidation and inflammation and stimulates neurogenesis in the APPswe/PS1ΔE9 mouse model of Alzheimer’s disease. 2013;8:e54769.

[23] Gregori M, Taylor M, Salvati E, Re F, Mancini S, Balducci C, et al. Retro-inverso peptide inhibitor nanoparticles as potent inhibitors of aggregation of the Alzheimer's Aβ peptide. 2017;13:723-32.
[24] Bansal S, Maurya IK, Yadav N, Thota CK, Kumar V, Tikoo K, et al. C-terminal fragment, Aβ32–37, analogues protect against aβ aggregation-induced toxicity. 2016;7:615-23.
[25] Hao J, Zhang W, Zhang P, Liu R, Liu L, Lei G, et al. Aβ20–29 peptide blocking apoE/Aβ interaction reduces full-length Aβ42/40 fibril formation and cytotoxicity in vitro. 2010;44:305-13.
[26] Santhoshkumar P, Sharma KKJM, biochemistry c. Inhibition of amyloid fibrillogenesis and toxicity by a peptide chaperone. 2004;267:147-55.
[27] Richman M, Wilk S, Chemerovski M, Wärmländer SK, Wahlström A, Gräslund A, et al. In vitro and mechanistic studies of an antiamyloidogenic self-assembled cyclic d, l-α-peptide architecture. 2013;135:3474-84.
[28] Austen BM, Paleologou KE, Ali SA, Qureshi MM, Allsop D, El-Agnaf OMJB. Designing peptide inhibitors for oligomerization and toxicity of Alzheimer's β-amyloid peptide. 2008;47:1984-92.
[29] Xie H, Qiao Z, Wang H, Duan H, Yang Y, Wang CJJoPS. Inhibition of β-amyloid peptide self-assembly and cytotoxicity by poly (LVFF-co-β-amino ester). 2015;21:608-14.
[30] Lemere CAJMn. Immunotherapy for Alzheimer's disease: hoops and hurdles. 2013;8:1-6.
[31] Tan W, Wang H, Chen Y, Zhang X, Zhu H, Yang C, et al. Molecular aptamers for drug delivery. Trends in biotechnology. 2011;29:634-40.
[32] Famulok M, Hartig JS, Mayer G. Functional aptamers and aptazymes in biotechnology, diagnostics, and therapy. Chemical reviews. 2007;107:3715-43.
[33] Navani NK, Li Y. Nucleic acid aptamers and enzymes as sensors. Current opinion in chemical biology. 2006;10:272-81.
[34] Crespi GA, Hermans SJ, Parker MW, Miles LA. Molecular basis for mid-region amyloid-β capture by leading Alzheimer's disease immunotherapies. Scientific reports. 2015;5:9649.
[35] Ultsch M, Li B, Maurer T, Mathieu M, Adolfsson O, Muhs A, et al. Structure of crenezumab complex with Aβ shows loss of β-hairpin. Scientific reports. 2016;6:1-11.
[36] Arndt JW, Qian F, Smith BA, Quan C, Kilambi KP, Bush MW, et al. Structural and kinetic basis for the selectivity of aducanumab for aggregated forms of amyloid-β. Scientific reports. 2018;8:1-16.
[37] Schneider L. A resurrection of aducanumab for Alzheimer's disease. The Lancet Neurology. 2020;19:111-2.
[38] Gazit E. Global analysis of tandem aromatic octapeptide repeats: The significance of the aromatic–glycine motif. Bioinformatics. 2002;18:880-3.
[39] Sevigny J, Chiao P, Bussière T, Weinreb PH, Williams L, Maier M, et al. The antibody aducanumab reduces Aβ plaques in Alzheimer's disease. Nature. 2016;537:50-6.
[40] Merrifield R. Solid-phase peptide synthesis. Advances in enzymology and related areas of molecular biology. 1969;32:221-96.
[41] Wüthrich KJEN. NMR with proteins and nucleic acids. 1986;17:11-3.
[42] Goddard T, Kneller D. SPARKY 3. University of California, San Francisco. 2004;15.
[43] Guntert P. Automated NMR structure calculation with CYANA. Methods in molecular biology (Clifton, NJ). 2004;278:353-78.
[44] Hutchinson EG, Thornton JMJPS. PROMOTIF—a program to identify and analyze structural motifs in proteins. 1996;5:212-20.
[45] Whitmore L, Wallace B. DICHROWEB, an online server for protein secondary structure analyses from circular dichroism spectroscopic data. Nucleic acids research. 2004;32:W668-W73.
[46] Walsh DM, Thulin E, Minogue AM, Gustavsson N, Pang E, Teplow DB, et al. A facile method for expression and purification of the Alzheimer's disease-associated amyloid β-peptide. The FEBS journal. 2009;276:1266-81.
[47] Long F, Cho W, Ishii Y. Expression and purification of 15N-and 13C-isotope labeled 40-residue human Alzheimer's β-amyloid peptide for NMR-based structural analysis. Protein expression and purification. 2011;79:16-24.
[48] Kneller D, Kuntz I. UCSF Sparky-an NMR display, annotation and assignment tool. Journal of Cellular Biochemistry: WILEY-LISS DIV JOHN WILEY & SONS INC 605 THIRD AVE, NEW YORK, NY 10158-0012; 1993. p. 254-.

[49] Williamson MPJPinmrs. Using chemical shift perturbation to characterise ligand binding. 2013;73:1-16.
[50] Teilum K, Kunze MBA, Erlendsson S, Kragelund BBJPS. (S) Pinning down protein interactions by NMR. 2017;26:436-51.
[51] Morris GM, Huey R, Lindstrom W, Sanner MF, Belew RK, Goodsell DS, et al. AutoDock4 and AutoDockTools4: Automated docking with selective receptor flexibility. 2009;30:2785-91.
[52] Trott O, Olson AJJJocc. AutoDock Vina: improving the speed and accuracy of docking with a new scoring function, efficient optimization, and multithreading. 2010;31:455-61.
[53] Schrödinger L. Maestro. New York, NY2018.
[54] Schrödinger L. The PyMOL Molecular Graphics System, Version 2.0.
[55] Jao S-C, Ma K, Talafous J, Orlando R, Zagorski MG. Trifluoroacetic acid pretreatment reproducibly disaggregates the amyloid β-peptide. Amyloid. 1997;4:240-52.
[56] Whitmore L, Wallace BA. Protein secondary structure analyses from circular dichroism spectroscopy: methods and reference databases. Biopolymers: Original Research on Biomolecules. 2008;89:392-400.
[57] Bodenhausen G, Ruben DJ. Natural abundance nitrogen-15 NMR by enhanced heteronuclear spectroscopy. Chemical Physics Letters. 1980;69:185-9.

Chapter III: Study of heparin-α-synuclein structural interaction

1. Introduction

Parkinson's disease (PD) is a long-term degenerative disorder of the central nervous system that mainly affects the motor system. PD is, along with Alzheimer's diseases, the most frequently diagnosed neurodegenerative disorder. Part of PD's clinical diagnosis is still today based on symptoms, such as muscle rigidity, bradykinesia (slow movement), and resting tremor.[1] When the patient shows the first sign of motor symptoms, massive damage to the neurons in the substantia nigra (loss of more than 29 %) has already happened.[2]

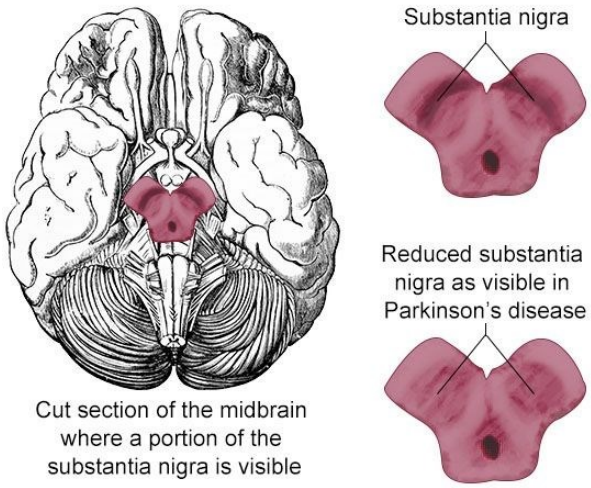

Figure 1. Cut-section of the midbrain in healthy and in Parkinson's disease.

The cause of cell degeneration in PD is currently still poorly understood but involves the formation of proteins into inclusions, named Lewy bodies (LB).[3] These can spread from pathological tissue regions to areas of newly grafted and healthy tissue,[4] causing damage and neuronal loss.[5-8] Among the proteins found in LB, α-synuclein (aSN) exerts a critical role in neurotoxicity.

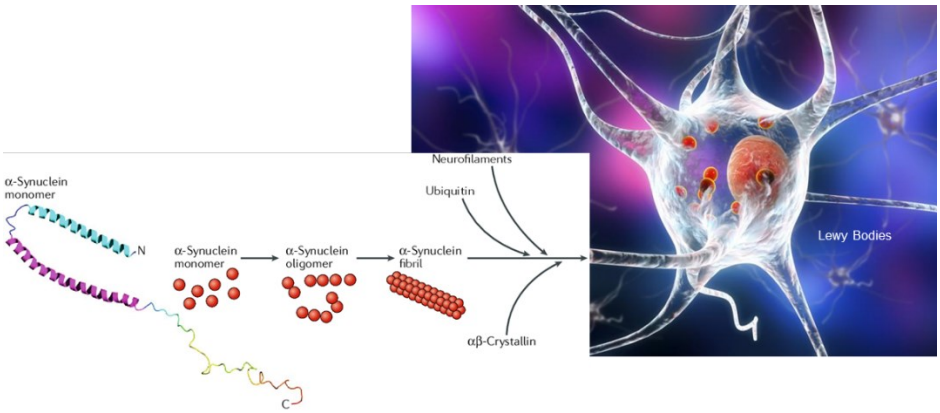

Figure 2. On the left, the pathway representing the aggregation of α-synuclein from its monomeric form to the formation of fibrils. On the right, a neuronal cell containing fibril aggregates of α-synuclein forming Lewy bodies.

1.1. α-synuclein

Three isoforms of synuclein, α, β, and γ, are known.[9, 10] α- and β-synuclein have presynaptic localization [11], whereas γ-synuclein is generally cytosolic.[12] The native functions of the synucleins are not well established. However, synucleins seem to be essential for the nervous systems' long-term,[13] and mice that were knockout for α, β, and γ-synuclein showed neural dysfunction typical of aged neurons and reduction in the synapse sizes.[13]

1.2.1. α-synuclein as monomer

aSN is composed of 140 amino acid residues:[11, 14, 15] 1-60 N-terminal fragment, also called[16] the amphipathic region, central, 61-95, known as the NAC region (non amyloid-β component), 96-140, C-terminal region, referred to as the acidic tail **(Figure 3)**.[14, 15] Seven imperfect unstructured KTK(E/Q)GV repeats are present in the N-terminal and NAC region; these undergo random coil to α-helical conformational changes triggered by cell membrane action.[17, 18] The lack of secondary structure for aSN classified it as an intrinsically disordered protein (IDP).

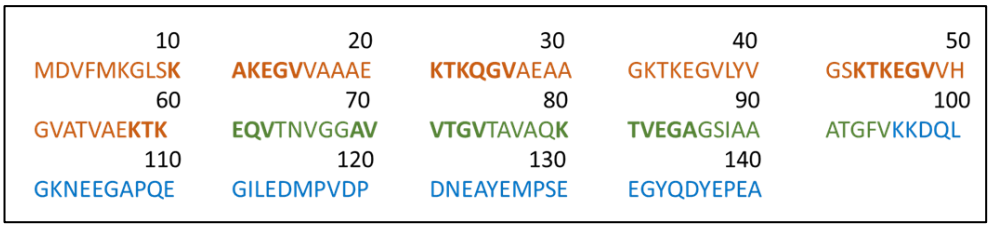

Figure 3. - The amino acid sequence of aSN. The N-terminal region is colored in orange, the NAC region is colored in green, and the C-terminal region is colored in blue. The seven KTK(E/Q)GV motifs are in bold writing.

aSN is abundant in the presynaptic terminals. Its reported cytosolic concentration typically ranges from 30-60 μM, and in some neurons, it makes up as much as 1% of the total cytosolic protein.[11] Multiple hypotheses have been proposed to account for the physiological role of aSN. It has been suggested that aSN i) can be a regulator of vesicular[19]transport,[20] ii) may affect the release of dopamine[21] iii) protect the cell from thermal and oxidative stress.[22] aSN is susceptible to the environment, particularly the balance of reactive oxygen species that changes with age.[23, 24] Moreover, the conformation of aSN is sensitive to chemical modification of several amino acids such as Met oxidation or Ser and Tyr[25-27] phosphorylation.[28] The in vivo concentration of aSN is far above the critical concentration for aggregation, indicating that aSN is kinetically metastable[29, 30], and aSN concentration in the neurons would have to be tightly regulated throughout evolution to prevent it from forming fibrils.[29]

1.2.2. α-synuclein fibrils

A shift in the aSN secondary structure (from random coil to β-sheet) leads to aggregation and fibril structure formation. The mature aSN fibrils form a polar structure composed of two twisting protofilaments with a parallel arrangement of their β-sheets.[19, 31, 32] The fibril core is highly ordered and is primarily composed of the NAC region, which contains many hydrophobic residues and short segments of the N- and C-terminal regions. It has been suggested that the negatively charged C-terminal region disfavor fibril formation due to repulsive interactions along with the positively charged KTK(E/Q)GV motifs. These are thought to be an evolutionary adaptation to protect against fibrillation.[33, 34] On the other hand, aggregates originating from residue ^{15}V-N^{65} of aSN, which span most of the N-terminal region and four residues of the NAC region, have been shown to display toxicity towards cells and act to stimulate the aggregation of full-length aSN.[35] Hence, this demonstrates that part of the N-terminal region and a part of the NAC region can indeed be fibrillated. Furthermore, if residues ^{71}V-T^{81} or ^{66}V-V^{74} are deleted, the fibrillation of aSN is

suppressed,[36, 37] suggesting the importance of the NAC region for aSN amyloid formation. Therefore, the cross-β core of aSN fibrils is formed by the NAC region, but recent high-resolution structures obtained by cryo-electron microscopy (EM) have shown that also part of the N-terminal partakes in the fibril β-structure.[31] Supported in part by solid-state nuclear magnetic resonance (NMR) spectroscopy, the fibril core structure was shown to include residues ^{38}L–V^{95}, revealing flexible structures for the N and C terminal extremities.[38] The pathological role of the N-terminal is not clear, but it is remarkable that all known single-point mutations related to PD locate to the N-terminal region (^{18}A-A^{53}) and not the NAC region.[39] While previous studies suggested the N-terminal as inhibitory for fibrillation,[34] recent studies have shown that N-terminal fragments, e.g., ^{15}V-N^{65}, can self-aggregate and, although the structural nature of these aggregates was not entirely determined, accelerate the aggregation of full-length aSN.[35]

1.3. Glycosaminoglycans (GAGs)

Amyloidogenic deposits in neurons are composed of glycosaminoglycans (GAGs) other than proteins.[40] Sulfated GAGs have been found related to Alzheimer's disease,[41-44] Creutzfeldt Jakob disease,[45] and PD.[46] By this evidence, GAGs are suggested to play an important role in amylogenesis. These molecules act interacting with fibrils through electrostatic interactions, and the degree of GAG sulphation of a is critical for fibril formation [47, 48], suggesting that the electrostatic interactions between GAGs and amyloid fibrils favor the amyloid formation. Heparan sulfate proteoglycans (HSPGs) have recently been found in Lewy bodies from PD patients.[46] Proteoglycans are glycosylated covalently with glycosaminoglycans (GAGs), which are linear unbranched polysaccharides [49, 50] playing physiological roles in cell-cell interaction.[51, 52] Also, fibrillar and aggregate uptake in the cell may occur via binding to HSPGs on the cell surface or selected glycosylated cell surface proteins;[53-55] thus, GAGs play a significant role in the spreading and further seeding of intracellular aggregation. In vivo, heparan sulfate has been shown to increase its sulfation level with age, leading to an age-dependent degree of sulfates.[56] From these molecules, one of the most sulfated GAGs is heparin [49], which is structurally closely related to heparan sulfate. It has been reported that heparin influences the fibrillation of aSN in a concentration-dependent manner through ionic interaction with the N-terminal[57, 58] or via the stabilization of a transition state favoring the β-sheet structure.[59] Furthermore, heparin has also been found integrated into fibrils.[58] Although the structural details are not known, heparin-induced fibrils of aSN have a different morphology compared to aSN fibrillated without heparin.[57-60] In addition, heparin may

induce the fibrillation of proteins that are not inherently found to fibrillate.[61, 62] To date, it has not been addressed which properties of GAGs and, in particular, heparin can modulate fibrillation.

2. Results

2.1. $aSN_{1–61}$ maintains disorder as in full-length aSN

To address if removing the NAC- and the C-terminal regions (residues 62–140) from aSN would impact the structural properties of $aSN_{1–61}$, we subjected it to biophysical analyses using SAXS, NMR, and CD spectroscopy. SAXS is a proper technique for determining the oligomeric states and quaternary structures of proteins in solution.

No concentration dependency of $aSN_{1–61}$ was observed in the concentration range used for SAXS data collection, and further analyses were based on the data collected at the highest concentration (573 μM, **Figure 4A**). The scattering curve and Kratky plot (**Figure 4A,B**) were consistent with that expected for an IDP. Using the EOM,[63] a pool of random chain structures based on the sequence of $aSN_{1–61}$ was generated, and an ensemble fitting of the experimental data was determined (**Figure 4A**). The selected ensemble indicated a high degree of flexibility in the protein, as the R_g distribution of the selected ensemble (**Figure 4C**) was almost as broad as the random pool. In addition, the distribution of the selected ensemble was skewed to the right, indicating $aSN_{1–61}$ to be extended compared to the random pool. The disordered state of $aSN_{1–61}$ was further confirmed with far-UV CD (**Figure 4D**). Thus, based on solution scattering and CD, the isolated N-terminal fragment, overall, retains a similar disorder to that of full-length aSN.

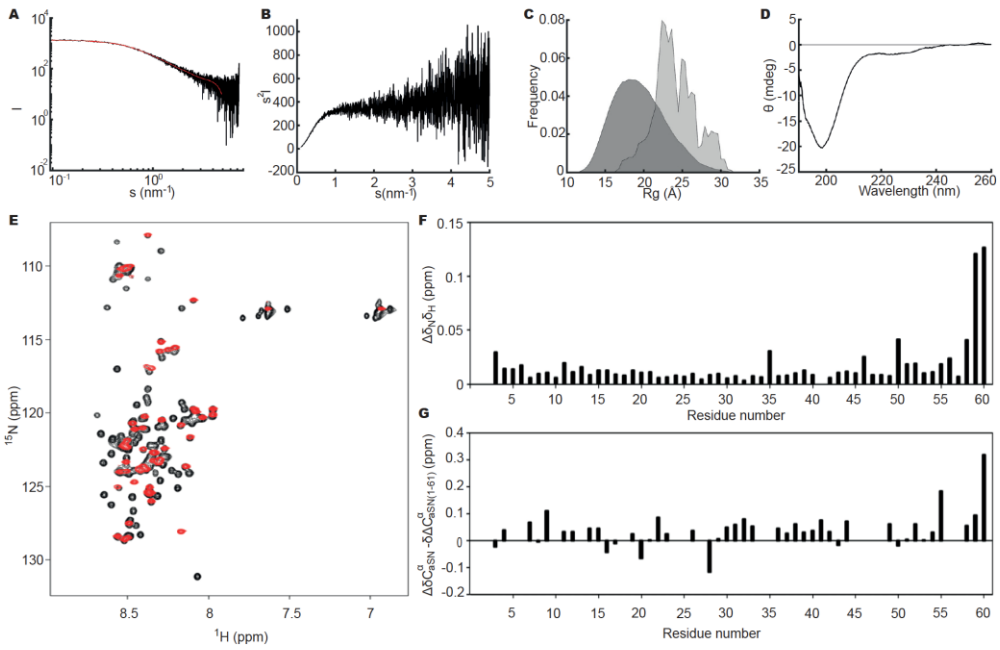

Figure 4. Structural studies of $aSN_{1–61}$. (**A**) Experimental small angle X-ray scattering (SAXS) data, relative scale, for $aSN_{1–61}$ (573 µM; black) and fit (red) obtained using ensemble optimization method (EOM) (χ^2 = 0.59). (**B**) Kratky plot of the SAXS data for $aSN_{1–61}$. (**C**) R_g distribution of the random pool (dark grey) and the selected ensemble (light grey) from EOM. (**D**) Far-UV CD spectrum for 10 µM $aSN_{1–61}$. (**E**) ^1H,^{15}N-HSQC spectra for ^{15}N-aSN (black) and ^{15}N-$aSN_{1–61}$ (red). (**F**) Amide chemical shift perturbations between aSN and $aSN_{1–61}$. (**G**) Differences in secondary chemical shifts of C^{α}, between aSN and $aSN_{1–61}$. Data from the C-terminal residues have been omitted for clarity.

Homonuclear and heteronuclear 3D NMR spectra were acquired to perform chemical shift assignment of aSN_{1-61} and compare the NMR structure of aSN_{1-61} with that of full-length aSN. Backbone chemical shift assignment was carried out by iteratively analyzing 3D ^1H,^{15}N-HSQC, HNCACB, HNCOCACB, HN(CA)CO, HNCO, and HN(CA)NNH spectra using CcpNMR software.[64] **Table 1** reports the ^1H, ^{13}C, and ^{15}N backbone chemical shift assignment of aSN_{1-61}

Table 1. ^1H, ^{13}C and ^{15}N backbone chemical shifts of aSN_{1-61}.

Residue	^1H	^{13}C	$^{13}C\alpha$	^{15}N
Met[1]	/	/	/	/
Asp[2]	/	/	/	/
Val[3]	8.29	176.76	62.63	120.51
Phe[4]	8.40	176.86	58.04	123.66
Met[5]	8.27	/	55.39	122.42

Lys[6]	8.32	175.58	/	122.74
Gly[7]	8.48	178.53	45.32	110.00
Leu[8]	8.11	175.05	55.20	121.62
Ser[9]	8.38	178.12	58.39	116.76
Lys[10]	8.43	176.24	56.27	123.78
Ala[11]	8.35	174.80	52.69	125.35
Lys[12]	8.40	176.22	56.50	120.96
Glu[13]	8.50	175.69	56.81	122.24
Gly[14]	8.52	178.70	45.32	110.19
Val[15]	8.03	176.05	62.65	120.29
Val[16]	8.36	176.72	62.51	125.45
Ala[17]	8.52	175.05	52.57	128.60
Ala[18]	8.38	174.81	52.77	123.81
Ala[19]	8.34	174.52	52.77	123.24
Glu[20]	8.39	175.80	56.80	120.24
Lys[21]	8.40	175.57	56.76	122.45
Thr[22]	8.21	178.04	62.36	115.55
Lys[23]	8.42	176.01	56.72	123.94
Gln[24]	8.50	176.11	56.23	121.82
Gly[25]	8.54	178.46	45.34	110.64
Val[26]	8.08	176.33	62.67	119.92
Ala[27]	8.49	174.57	52.85	127.52
Glu[28]	8.47	176.05	56.88	120.67
Ala[29]	8.36	174.98	52.74	125.03
Ala[30]	8.30	174.26	52.84	123.19
Gly[31]	8.37	178.54	45.34	107.88
Lys[32]	8.17	175.71	56.26	120.81
Thr[33]	8.30	178.06	61.95	115.82
Lys[34]	8.54	176.19	56.58	124.05
Glu[35]	8.51	175.79	56.88	122.03
Gly[36]	8.51	178.73	45.29	110.13
Val[37]	7.97	176.79	62.39	119.71
Leu[38]	8.35	176.08	55.01	126.01
Tyr[39]	8.34	177.16	57.93	122.65
Val[40]	8.14	176.62	62.20	123.63
Gly[41]	/	/	/	/
Ser[42]	8.32	/	58.41	115.72

Lys[43]	8.55	175.86	56.43	123.57
Thr[44]	8.25	178.13	61.93	115.69
Lys[45]	8.50	176.02	56.56	123.98
Glu[46]	8.51	175.79	56.96	122.28
Gly[47]	8.50	178.89	45.30	109.94
Val[48]	7.97	176.74	62.34	120.09
Val[49]	8.37	176.88	62.16	125.39
His[50]	8.56	176.87	56.40	125.00
Gly[51]	8.47	178.96	45.23	110.70
Val[52]	8.09	176.80	62.03	119.70
Ala[53]	8.56	174.91	52.44	128.38
Thr[54]	8.29	178.25	61.90	115.16
Val[55]	8.31	176.99	62.16	123.42
Ala[56]	8.29	175.09	52.48	128.48
Glu[57]	8.45	176.26	56.51	121.09
Lys[58]	8.51	175.96	56.32	123.33
Thr[59]	8.35	178.45	62.14	115.16
Lys[60]	8.46	177.18	56.37	124.74
Glu[61]	8.17	/	58.11	128.05

First, the $^{1}H,^{15}N$-HSQC spectra of aSN and $aSN_{1–61}$ were compared (**Figure 4E**), revealing that the vast majority of the peaks of $aSN_{1–61}$ overlaid those of full-length aSN. The assignment of the $aSN_{1–61}$ resonances revealed that besides effects from the negative charge at the new C-terminal, only small perturbations of the amide shifts were seen relative to full-length aSN (**Figure 4F**). When comparing the assigned secondary chemical shifts (SCS) of C^{α} for $aSN_{1–61}$ to those for aSN (**Figure 4G**), the SCSs of aSN were generally only slightly more positive. This may suggest a redistribution of the ensemble towards a less α-helical structure, i.e., a more extended chain, although the small amplitude together with the small perturbations for the amide shifts suggest this to be modest. A slight redistribution may likely be caused by the removal of long-range ionic interactions previously observed between the negatively charged C-terminal and the positively charged N-terminal.[65] Thus, also at the residue level, $aSN_{1–61}$ is as disordered as full-length aSN.

DOSY NMR experiments were performed to monitor the dynamic differences of the two molecules. We measured the diffusion coefficients of $aSN_{1–61}$ and aSN and calculated their hydrodynamic radius R_h to be 20.1 and 29.1 Å, respectively (**Table 2**). A recent method

published by Nygaard et al.[66] provides information on the extendedness of the chain from the ratio of R_g/R_h. A similar ratio of 1.2 for both $aSN_{1–61}$ and aSN (**Table 2**) suggested comparable extendedness for the chains.

In conclusion, the free 61 N-terminal residues of aSN represent a fully disordered but slightly extended chain that maintains most full-length properties. Likely due to the removal of the acidic C-terminal, the chain becomes, on average, slightly more accessible than the full-length counterpart.

Table 2. Hydrodynamic radius and radius of gyration of aSN and $aSN_{1–61}$.

		Radii (Å)		
		aSN	$aSN_{1–61}$	Reference
R_g	Folded	14.4	10.5	[67]
	Unfolded	36.8	22.4	[68]
	SAXS	36.5	24.0 ± 0.3	[69], This work
R_h	Folded	20.1	15.8	[70]
	Unfolded	36.8	22.9	[70]
	IDP	31.1	20.3	[71]
	NMR*	29.1 ± 0.1	20.1 ± 0.1	This work
R_g/R_h	Folded	0.71	0.66	[67]
	Unfolded	1	0.97	[68]
	Nygaard	0.98	1.05	[66]
	SAXS/NMR	1.08	1.2	This work

*: Errors from fit.

2.2. Heparin Binds Weakly but Preferably to $aSN_{1–61}$

As previously mentioned, heparin may have a role in inducing $aSN_{1–61}$ fibrillation.[72] To perform a structural investigation of the interaction, we mapped out interaction sites by titrating heparin into ^{15}N-$aSN_{1–61}$ and ^{15}N-aSN. Heparin was added in 7-times excess (1:7) to ^{15}N-$aSN_{1–61}$. (**Figure 5A).** The CSPs were most pronounced for residues ^{5}M–E^{13} but were also substantial for residues in an apparent pattern along the chain (**Figure 5A**). The CSP analysis suggested that the KTK motifs were involved in but not solely responsible for the interaction, as also hydrophobic residues such as Met, Val, and Ala were perturbed. As the populations of free and bound states were in fast exchange on the NMR timescale, we could follow the peak position as a function of added heparin and extract a K_D for heparin-binding to $aSN_{1–61}$ of 233 ± 40 μM (**Figure 5C,D**). Furthermore, we measured the diffusion of $aSN_{1–}$

$_{61}$ in the presence of heparin, revealing an increased R_h of 29.6 ± 1.0 Å from the 20.0 ± 0.1 Å of the free aSN$_{1–61}$, supporting the binding of heparin to aSN$_{1–61}$.

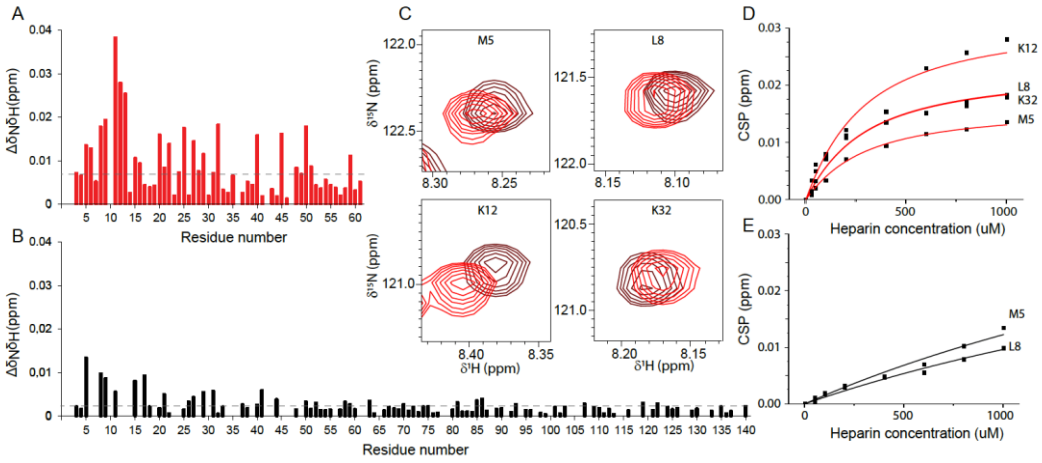

Figure 5. aSN and heparin interaction. (**A**) Amide chemical shift perturbations (CSPs) of aSN$_{1–61}$ upon addition of heparin (1:7); the black line represents the average CSPs. (**B**) Amide CSPs of aSN upon addition of heparin (1:10); the red line represents the average CSPs. (**C**) Zoom on the peak positions of specific residues of aSN$_{1–61}$ in the absence (red) and presence (brown) of heparin. (**D**) CSPs of the most perturbed residues of aSN$_{1–61}$ as a function of added heparin. The solid line represents a fit to a one-site binding model. (**E**) CSPs of aSN upon addition of heparin as a function of added heparin. The solid line represents a fit to a one-site binding model as described in.[73]

The addition of a 10-times molar excess of heparin to full-length aSN resulted in much smaller CSPs than those seen with aSN$_{1–61}$, suggesting a preference for heparin to bind to the truncated aSN$_{1–61}$ **(Figure 5B)**. No CSP saturation was achieved for aSN, and hence, no K_D was determined (**Figure 5E**).

In summary, heparin binds weakly to aSN$_{1–61}$, mainly within the N-terminal 15 residues, and prefers aSN$_{1–61}$ to full-length aSN, likely because of increased access to the N-terminal residues.

2.3. Heparin and aSN$_{1–61}$ co-exist in the fibrils

We next addressed if heparin co-fibrillates with aSN$_{1-61}$ using wide-field fluorescence microscopy. To test for any nonspecific binding, the fibrils of both aSN$_{1-61}$ (formed in the presence of heparin) and aSN (formed in the absence of heparin) were subjected to secondary immunostaining towards heparin. The fibrils were visualized by ThT fluorescence, while the presence of heparin was detected by a secondary antibody (2'Ab) conjugated to Alexa Flour^{TM} 647 (**Figure 6A**). While the aSN fibrils, visible in the ThT channel as large clusters

and smaller fibrils, showed no signal in the heparin channel (**Figure 6A**, bottom), the aSN_{1-61} fibrils induced by the presence of heparin exhibited a distinct signal, confirming co-existence in the fibril. This signal was mostly overlapping with that of ThT (**Figure 6A**, top). While the large clusters of fibril material (diameter > 5 µm) showed a uniform but diffuse signal of co-localized heparin, the smaller clusters (5 µm < diameter > 1 µm) were decorated by a punctate and brighter pattern (**Figure 6 A,B**). This feature was further pronounced in the smallest of the visible assemblies (diameter > 350 nm), where bright dots of heparin were found scattered along the axis of the fibrils (**Figure 6B**). Based on threshold images, the Manders' Colocalization Coefficients were determined for the fractional overlap of ThT with heparin, M1, and heparin with ThT, M2, (**Figure 6C**). Here, 37 ± 11% of the ThT signal co-localized with heparin, with the additional ThT signal, observed either being a result of heparin removed in the washing steps, or the presence of fibrils consisting only of aSN_{1-61}. In the latter case, this could be a result of secondary nucleation and seeding effects by the co-fibrils. The heparin signals co-localized fully with ThT.

Taken together, these results suggest that heparin coexists with aSN_{1-61}in the fibrils.

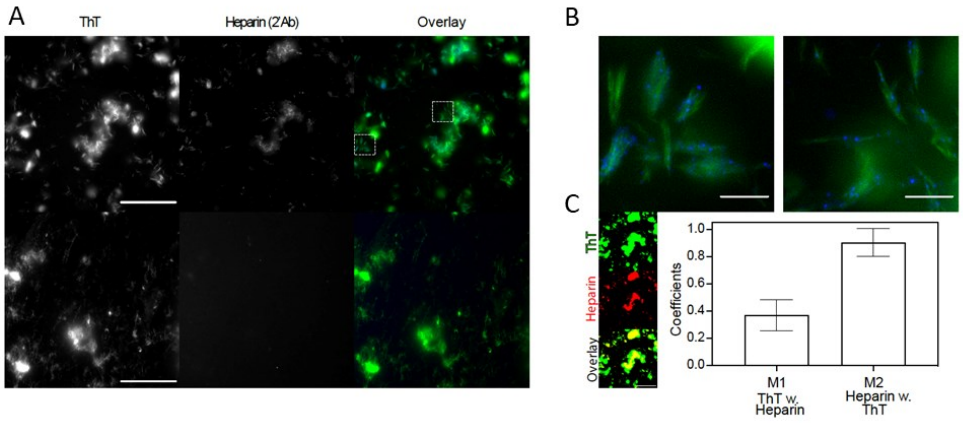

Figure 6. (**A**) Wide-field fluorescence microscopy images of (top) aSN_{1-61} fibrils produced in the presence of heparin (1:1.3 molar ratio) and (bottom) aSN fibrils produced in the absence of heparin. The (left) ThT signal from the fibrils is shown alongside the (middle) Alexa Flour 647 signal from immunostained heparin and the (right) overlay with highlighted regions of interest (ROIs). Scale bars are 50 µm. (**B**) Zoom of the ROIs from the overlay in (**A**). Scale bars are 5 µm. (**C**) Example threshold images of ThT (green, top), heparin (red, middle) and overlay (bottom) used to calculate the depicted Manders' Colocalization Coefficients (means ± s.d., n = 10) of M1 (ThT with heparin) and M2 (heparin with ThT). Scale bar in the threshold image examples are 50 µm.

2.4. $aSN_{1–61}$/Heparin co-fibrils seed fibrillation of full-length aSN

Having established that the presence of heparin leads to $aSN_{1–61}$ co-fibril formation, we also investigated if the co-fibrils could induce further fibrillation of both full-length aSN and $aSN_{1–61}$. Co-fibrils formed from $aSN_{1–61}$/heparin at a molar ratio of 1:1.7 ($aSN_{1–61}$ 200 μM, heparin 333 μM) were therefore used as seeds. For $aSN_{1–61}$, controls without seeds followed the previous observations with fibrillation after ~100 h in the presence of heparin and no fibrillation in the absence of heparin (**Figure 7A**). With $aSN_{1–61}$ in the presence of co-fibril seeds and with co-fibril seeds and additional free heparin, we observed no lag phase but a continued increase in ThT fluorescence directly from the initiation of the experiment (**Figure 7A**). Upon seeding, the direct entrance into the elongation phase is consistent with $aSN_{1–61}$ fibrillating into further (co-)fibril material with additional heparin. As this was also observed without additional free heparin (**Figure 7A**), $aSN_{1–61}$ fibrillation seeded by co-fibril material may also occur without incorporating heparin, consistent with the surplus ThT signal observed in the wide-field fluorescence microscopy. The maximum ThT fluorescence was reached after ~75 and ~20 h, respectively, the increase being fastest with additional heparin present. This difference in growth rate further underlines that heparin facilitates the growth of the fibrils. Finally, the secondary structure of $aSN_{1–61}$ under the four conditions was investigated. At the end-point of the fibrillation assays, the samples with co-fibril seeds and/or heparin all had a β-sheet structure with a minimum at ~220 nm and a maximum at ~198 nm, although some smaller variations in minimum wavelength were visible. $aSN_{1–61}$ without seeds or heparin remained disordered (**Figure 7C**). The kinetic profiles of the unseeded aSN fibrillated alone and with heparin revealed a similar maximum ThT fluorescence (**Figure 7B**) and a decreased lag phase in the presence of heparin, consistent with the accelerating effect of heparin observed previously.[57, 58] When aSN was fibrillated in the presence of $aSN_{1–61}$/heparin co-fibril seeds without and with additional free heparin, we observed a shortening of the lag phase to ~30 h and a three-fold increase in the final ThT value compared to those observed in the un-seeded conditions (**Figure 7B**). In contrast, the presence of additional free heparin did not alter the kinetics in the seeded conditions. The increased ThT signal in the seeded conditions indicates differences in the amount of fibrillated material or in fibril morphology with differences in the binding of ThT compared to that in the unseeded conditions. In all four end-point conditions, a β-sheet structure was confirmed by CD. The β-sheet structure was more pronounced for aSN fibrillated with co-fibril seeds (**Figure 7D**).

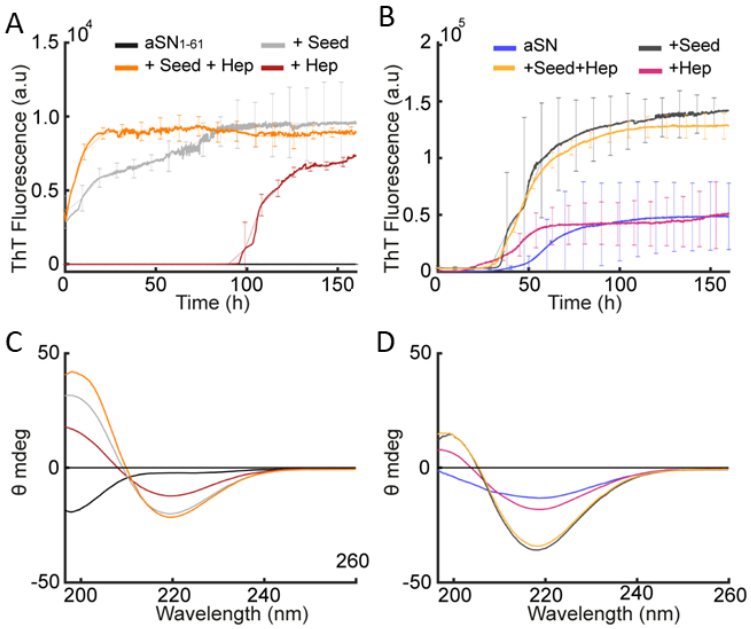

Figure 7. Seeding with $aSN_{1–61}$/heparin co-fibrils. (**A**) ThT assays for $aSN_{1–61}$ (black), $aSN_{1–61}$ with heparin (red), $aSN_{1–61}$ with co-fibril seeds (grey), and $aSN_{1–61}$ with co-fibril seeds and heparin (orange). (**B**) ThT assay for aSN (blue), aSN with heparin (magenta), aSN with co-fibril seeds (dark grey), and aSN with co-fibril seeds and heparin (yellow). Note that the y-axis ranges depicted differ for the two fibrillation assays (**A** and **B**). (**C**) Far-UV CD spectra of $aSN_{1–61}$, $aSN_{1–61}$ with heparin, $aSN_{1–61}$ with cofibril seeds, and $aSN_{1–61}$ with co-fibril seeds and heparin (colors as in **A**). (**D**) Far-UV CD spectra of aSN, aSN with heparin, aSN with co-fibril seeds, and aSN with co-fibril seeds and heparin (colors as **B**).

3. Conclusions

We showed that heparin binds directly to the N-terminal end of $aSN_{1–61}$ and does so with a higher affinity than full-length aSN. While we did not observe fibrillation of $aSN_{1–61}$ on its own, we intriguingly also observed heparin-induced fibrillation of $aSN_{1–61}$ and detected heparin as a co-existing partner of the fibrils. The co-existing fibrils of $aSN_{1–61}$/heparin accelerated the fibrillation of full-length aSN as well as the further fibrillation of $aSN_{1–61}$. In addition, our data suggest that no individual property of heparin but rather the combined physical and chemical characteristics affect the structure of aSN by inducing type I β-turn structures, which may be critical for triggering aSN fibrillation.

By removing the complexity arising from the process of aSN fibrillation by focusing on the $aSN_{1–61}$ variant, we observed direct binding of heparin to the N-terminal ~50 residues of aSN. The $aSN_{1–61}$ variant did not possess intrinsic fibrillation potential, but heparin could act as a promoter for initiating fibrillation via the induction of type-I β-turn structures in the aSN N-terminal.

These structures were observed by CD spectroscopy through a distinct ellipticity profile. Heparin co-existed with $aSN_{1–61}$ in the formed fibrils, likely in the form of a structural scaffold, and the co-fibrils seeded additional fibrillation even in the absence of free heparin, as well as of full-length aSN, resulting in fibrils with a potentially different morphology compared to that of fibrils formed by aSN alone. Thus, small amounts of heparin, or more likely that in the form of aged heparan sulfate with an increased level of sulfation, present in Lewy bodies of PD patients, can potentially initiate a cascade of fibrillation-relevant events.

4. Materials and Methods

4.1. Compounds

Heparin was purchased from Iduron (HEP001). It was dissolved in 50 mM sodium phosphate, pH 7.4, with 0–500 mM NaCl and stored at 4 ◦C for a maximum of two days before use. Chondroitin sulfate A from bovine trachea and β-casein from bovine milk were purchased from Sigma-Aldrich (C9819 and C6905, Søborg, Denmark).

4.2. Expression and Purification of Recombinant $aSN_{1–61}$

A pET-11a vector with an insert for His-SUMO-$aSN_{1–61}$ was purchased from GenScript® (Leiden, Netherlands). BL21 (DE3) E. coli cells were heat-shock transformed with the plasmid, incubated in Super Optimal Broth medium for 1 h, and plated on agar containing 1:1000 ampicillin (100 mg/mL). The plates were incubated overnight at 37 °C, and preheated Luria Bertani (LB) medium (50 mL) with 1:1000 ampicillin (100 mg/mL) was inoculated with one colony and incubated overnight at 37 °C and 200 rpm. Glycerol stocks were made from the overnight culture by mixing them 1:1 (volume) with 86% (v/v) sterile glycerol, aliquoted in 0.5 mL, and stored at −80 °C. For expression, an aliquot of 2 µL of the glycerol stock, or a colony from the agar plate, was transferred to preheated LB medium with 1:1000 of ampicillin (100 mg/mL) and incubated overnight at 37 °C and 200 rpm. The LB expression cultures, each 1 L, contained 1:1000 of ampicillin (100 mg/mL) and were inoculated with 1:100 of the overnight culture and incubated at 37 °C and 200 rpm. The expression of His-SUMO-$aSN_{1–61}$ was induced with 1:1000 of IPTG (1 M) at OD_{600} = 0.5-0.6. The cells were harvested 2 h after induction by centrifugation at 4801× g for 20 min at 4 °C. The cells were dissolved in 30 mL of buffer A (50 mM Tris, 150 mM NaCl, 10 mM Imidazole, pH 8) per L of expression medium. The cell pellet was stored at -20 °C until purification. The resuspended cell pellet was lysed by six cycles of thawing and freezing in liquid nitrogen. The lysed cells were centrifuged at 25,515× g for 20 min at 4 °C. The supernatant was loaded onto a 5 mL HisTrap FF column (GE healthcare, Chicago, IL, USA)

equilibrated in buffer A with a flow of 1 mL/min. His-SUMO-aSN$_{1–61}$ was eluted from the column using a step gradient with imidazole-10, 200, and 500 mM imidazole-with at flow of 2 mL/min. Fractions of 5 mL were collected and analyzed by SDS-PAGE, fractions containing His-SUMO-aSN$_{1–61}$ were pooled, and 0.5–1 mL of 10 µM His-ULP1 was added (see below for production details). The solution with His-SUMO-aSN$_{1–61}$ and His-ULP1 was subsequently dialyzed overnight at 4 °C in 50 mM Tris, 150 mM NaCl, 10 mM imidazole, 1 mM 2-mercaptoethanol, pH 8, in dialysis bags with a cut-off of 3.5 kDa. The dialysate was loaded onto a HisTrap FF column equilibrated in buffer A. The flow-through containing the cleaved aSN$_{1–61}$ was collected in fractions of 5 mL. aSN$_{1-61}$ was dialyzed into 50 mM Tris, 10 mM NaCl, pH 8.5, using a cut-off of 3.5 kDa. The dialysate was loaded onto an HiTrap FF SP 5 mL column (GE healthcare), equilibrated with 50 mM Tris, 10 mM NaCl, pH 8.5, and aSN$_{1–61}$ was eluted with a 0–100% step gradient to 0.5 M NaCl using a flow rate of 1 mL/min. aSN$_{1–61}$ was collected in fractions of 0.5 mL. Afterwards were the fractions with aSN$_{1–61}$ dialyzed overnight at 4 °C in a 50 mM sodium phosphate buffer, 150 mM NaCl, pH 7.4, with a Spectra-Por® Float-A-Lyzer® G2 (Merck, Darmstadt, Germany), with a cutoff of 3.5 kDa. The concentration of aSN$_{1–61}$ was determined using a Pierce™ BCA Protein Assay Kit (ThermoFisher 23225, Denver, CO, USA), following the standard protocol for microplate mode. Incubation and measurements were performed using a FLUOstar OMEGA plate reader (BMG LABTECH, Orthenberg, Germany). The identity of the purified aSN$_{1–61}$ was confirmed by amino acid analysis by ALPHALYSE™ (Odense, Denmark).

4.3. Purification of Full-Length Recombinant aSN

The purification of full-length aSN was essentially performed as previously described [34] with a few modifications. Briefly, aSN was expressed in LB medium with 1:1000 ampicillin (100 mg/mL), and protein expression was induced at OD_{600} = 0.6. The cells were harvested after 3 h at 4801× g, and the cell pellet was resuspended and stored at -20 °C. The cells were lysed with osmotic shock, and non-thermostable proteins were removed by boiling and centrifugation. The supernatant was dialyzed overnight in 20 mM Na_2HPO_4, 2.5 mM EDTA at pH 6.5. The dialyzed solution was filtered through a 0.45 µm filter and loaded onto a 5 mL HiTrap Q FF column (GE healthcare, Chicago, IL, USA) equilibrated in 20 mM Na_2HPO_4, 2.5 mM EDTA at pH 6.5. aSN was eluted by a linear gradient with a final salt concentration of 0.5 M NaCl. Fractions containing aSN were pooled and loaded onto a Superdex 200 size exclusion column 120:100 (GE Healthcare, Chicago, USA), which was equilibrated in 50 mM Na_2HPO_4, 150 mM NaCl, pH 7.4. Fractions containing aSN were

pooled at stored at -80 °C. Before the experiments, aSN was dialyzed with a cut-off of 3.5 kDa into 50 mM sodium phosphate, 150 mM NaCl, pH 7.4.

4.4. Expression and Purification of Recombinant His-ULP1

His6-tagged ULP1 was purified as described in Prestel et al., 2019.[74]

4.5. Protein Fibrillation Assay

Thioflavin T (ThT) detected fibrillation assays were conducted using a FLUOstar OMEGA plate reader (BMG LABTECH, Orthenberg, Germany). Bottom–bottom mode was applied with excitation at 450 ± 5 nm, and emission at 480 ± 5 nm was measured. The concentration of $aSN_{1–61}$ was 100 or 200 μM, and for aSN, a concentration of 83 μM (1.2 mg/mL) was used. Varying molar ratios of heparin were included as denoted in the results. In general, all assays were performed in 50 mM NaP, 150 mM NaCl, while a few additional tests were performed in 1 M NaCl, 160 mM $(NH_4)_2SO_4$ or in the presence of β-casein to decipher the influence of heparin. Samples including 20 μM ThT were placed in NUNC 96-well optical polymer-based black plates (ThermoFisher 265301, Denver, USA) with a total volume of 150 μL per well and sealed with clear polyolefin tape (ThermoFisher 232702, Denver, CO, USA). The fluorescence was measured every 6 min, in repeated cycles, with orbital shaking (700 rpm) for 280 s of each 360 s cycle. The assays were run at 37 °C for a total of 7 days.

4.6. Seeding Experiments

Seed fibrils of aSN1–61/heparin was prepared as described above ($aSN_{1–61}$ 200 μM, heparin 333 μM). Subsequently, fibrillation assays for full-length aSN (60 μM) and $aSN_{1–61}$ (200 μM) were performed under four different conditions: (i) in the presence of 10% (v/v) seed fibrils; (ii) in the presence of heparin (33 μM); (iii) in the presence of 10% (v/v) seed fibrils and additional free heparin (33 μM), i.e., a mix of conditions (i) and (ii); and lastly, as control, (iv) aSN and $aSN_{1–61}$ alone, respectively.

4.7. Circular Dichroism (CD)

A Jasco J-1500 CD spectropolarimeter (Jasco, Easton, PA, USA) was used with the following settings: spectral width, 260–190 nm; data pitch, 0.1 mm; scanning speed, 50 nm/min; band width, 1 mm; temperature, 25 °C. A quartz cuvette of 0.1 mm was used, and each spectrum was an accumulation of three scans. Samples before and after the fibrillation assays were diluted to concentrations in the range of 15–20 μM. Background spectra of the buffers (50 mM sodium phosphate (NaP), 150 mM NaCl, pH 7.4, or 50 mM NaP, 1 M NaCl, pH 7.4) were collected at identical settings and subtracted.

4.8. Small Angle X-ray Scattering (SAXS)

SAXS data were collected at the beamline P12[75] operated by EMBL at the Petra III storage ring (DESY, Hamburg, Germany). Data were collected for $aSN_{1–61}$ (223–573 µM) in 50 mM NaP, 150 mM NaCl, pH 7.4 at 8 °C, and for heparin (33–333 µM) in several different buffer conditions: 50 mM NaP with 0–500 mM NaCl pH 7.4, or 50 mM Tris with 0–500 mM NaCl, pH 7.4, at room temperature. The automated sample changer was used with a sample loading volume of 30 µL and sample flow and exposure time of 0.495 s/frame, with 40 frames collected per sample. The scattering profiles of matching buffers were measured before and after each sample. Initial data reduction was performed using the SASFLOW pipeline,[76] and primary data analysis was subsequently conducted in PRIMUS.[77] The ensemble optimization method (EOM)[63] was employed to model the conformational ensemble of $aSN_{1–61}$. A fit to the experimental data was obtained through selection from a random pool of 10,000 structures generated based on the sequence, using default parameters with native-like chains.

4.9. NMR Sample Preparation

For NMR analyses, full-length aSN or $aSN_{1–61}$ was expressed and purified in M9 minimal medium with the addition of $^{15}NH_4Cl$ (and $^{13}C_6$-glucose when needed).[78] After dialysis into 20 mM Na_2HPO_4, 150 mM NaCl, pH 7.4, the samples were added to 10% (v/v) D_2O, 0.02% (w/v) sodium azide (NaN_3), and 0.7 mM 4,4-dimethyl-4-silapentane-1-sulfonic acid (DSS). For the acquisition of spectra for the backbone assignment of $^{13}C,^{15}N$-$aSN_{1–61}$, the protein concentration was 0.5 mM. For measurements of the hydrodynamic radii (R_h) of ^{13}C-^{15}N-$aSN_{1–61}$ and full-length ^{15}N-aSN, a sample concentration of 0.1 mM protein with 0.2% 1,4-dioxane added as an internal reference was used. The interaction of $^{13}C,^{15}N$-$aSN_{1–61}$ with heparin was evaluated by monitoring the changes in chemical shifts using solutions of 0.1 mM $^{13}C,^{15}N$-$aSN_{1–61}$ prepared in duplicate. To one solution, 1 mM heparin was added. Using the two solutions, different molar ratios of $^{13}C,^{15}N$-$aSN_{1–61}$/heparin (1:0, 1:0.3, 1:0.5, 1:1, 1:2, 1:4, 1:6, 1:8 and 1:10) were obtained. Similar titration was performed with ^{15}N-aSN using aSN/heparin ratios of (1:0, 1:0.5, 1:1, 1:2, 1:4, 1:6, 1:8 and 1:10) and an aSN concentration of 0.1 mM.

4.10. NMR Data Recording and Processing

All NMR spectra were acquired at 10 °C (283 K) on a Bruker AVANCE III 600MHz (^1H) spectrometer equipped with a cryogenic probe. The spectra were transformed and visualized in Topspin (Bruker, Fälladen, Switzerland) and analyzed using the CcpNMR Analysis

software.[64] Assignments of the backbone nuclei of $^{13}C,^{15}N$-$aSN_{1–61}$ were performed manually from the analysis of $^{1}H,^{15}N$-HSQC, HNCACB, HNCOCACB, HN(CA)CO, HNCO and HN(CA)NNH spectra acquired with non-uniform sampling[79] using standard pulse sequences. Proton chemical shifts were referenced internally to DSS at 0.00 ppm, with heteronuclei referenced by relative gyromagnetic ratios. Diffusion constants were acquired by diffusion ordered spectroscopy (DOSY) experiments.[80] A total of 32 spectra with gradient strengths ranging from 2% to 98% of the maximum value were recorded. A diffusion time Δ of 200 ms and gradient length δ of 2 ms were used in all the experiments. The pseudo 2D data were Fourier transformed, baseline corrected in Topspin and subsequently analyzed in Dynamics Center (Bruker, Fälladen, Switzerland). The diffusion constants were determined by the fitting of peak intensity decays using the Stejskal-Tanner equation[81]:

$$I = I_0 e^{-g^2\gamma^2\delta\hat{}2\left(\Delta-\frac{\delta}{3}\right)D}$$

where I is the intensity, g is the gradient strength, γ is the gyromagnetic ratio of ^{1}H, and D is the diffusion constant. 1,4-dioxane with a known hydrodynamic radius of 2.12 Å was used as an internal reference and used for the calculation of R_h according to Wilkins et al.[70]:

$$R_{\mathrm{h,prot}} = \frac{D_{\mathrm{ref}} \cdot R_{\mathrm{h,ref}}}{D_{\mathrm{prot}}}$$

where D_{ref} and $R_{h,ref}$ are the diffusion and the hydrodynamic radius of the internal reference, respectively, and D_{prot} and $R_{h,prot}$, the diffusion and the hydrodynamic radius of the protein. For chemical shift perturbation (CSP) analysis, ^{1}H-^{15}N-HSQC spectra of aSN_{1-61} free and with increasing concentrations of heparin were recorded and analyzed. Chemical shift perturbations (CSPs) were analyzed as combined amide chemical shift changes following the expression:

$$\Delta\delta_{NH}(ppm) = \sqrt{(\Delta\delta\ ^{1}H)^2 + (0.154 * \Delta\delta^{15}N)^2}$$

The determination of the binding affinity, K_D, from changes in chemical shift was performed as described[73] using the series of $^{1}H,^{15}N$-HSQC spectra recorded for free $aSN_{1–61}$ and with increasing heparin concentration. The content of the transient structure in $aSN_{1–}$

$_{61}$ was evaluated from secondary C α-chemical shifts using a random coil reference set for intrinsically disordered proteins.[82-84]

References

[1] Goedert MJNRN. Alpha-synuclein and neurodegenerative diseases. 2001;2:492-501.
[2] Greffard S, Verny M, Bonnet A-M, Beinis J-Y, Gallinari C, Meaume S, et al. Motor score of the Unified Parkinson Disease Rating Scale as a good predictor of Lewy body–associated neuronal loss in the substantia nigra. 2006;63:584-8.
[3] Trétiakoff CJTdP. Contribution a l'etude de l'Anatomie pathologique du Locus Niger de Soemmering avec quelques deduction relatives a la pathogenie des troubles du tonus musculaire et de la maladie de Parkinson. 1919.
[4] Spillantini MG, Schmidt ML, Lee VM-Y, Trojanowski JQ, Jakes R, Goedert MJN. α-Synuclein in Lewy bodies. 1997;388:839-40.
[5] Lewy FHJPaHdn. Paralysis agitans. I. 1912.
[6] Ma SY, Röyttä M, Rinne JO, Collan Y, Rinne UKJJotns. Correlation between neuromorphometry in the substantia nigra and clinical features in Parkinson's disease using disector counts. 1997;151:83-7.
[7] Ross GW, Petrovitch H, Abbott RD, Nelson J, Markesbery W, Davis D, et al. Parkinsonian signs and substantia nigra neuron density in decendents elders without PD. 2004;56:532-9.
[8] Kordower JH, Chu Y, Hauser RA, Freeman TB, Olanow CWJNm. Lewy body–like pathology in long-term embryonic nigral transplants in Parkinson's disease. 2008;14:504-6.
[9] Jakes R, Spillantini MG, Goedert MJFl. Identification of two distinct synucleins from human brain. 1994;345:27-32.
[10] Lavedan C, Leroy E, Dehejia A, Buchholtz S, Dutra A, Nussbaum RL, et al. Identification, localization and characterization of the human γ-synuclein gene. 1998;103:106-12.
[11] Iwai A, Masliah E, Yoshimoto M, Ge N, Flanagan L, De Silva HR, et al. The precursor protein of non-Aβ component of Alzheimer's disease amyloid is a presynaptic protein of the central nervous system. 1995;14:467-75.
[12] Buchman VL, Hunter HJ, Pinõn LG, Thompson J, Privalova EM, Ninkina NN, et al. Persyn, a member of the synuclein family, has a distinct pattern of expression in the developing nervous system. 1998;18:9335-41.
[13] Greten-Harrison B, Polydoro M, Morimoto-Tomita M, Diao L, Williams AM, Nie EH, et al. αβγ-Synuclein triple knockout mice reveal age-dependent neuronal dysfunction. 2010;107:19573-8.
[14] Weinreb PH, Zhen W, Poon AW, Conway KA, Lansbury PTJB. NACP, a protein implicated in Alzheimer's disease and learning, is natively unfolded. 1996;35:13709-15.
[15] Uéda K, Fukushima H, Masliah E, Xia Y, Iwai A, Yoshimoto M, et al. Molecular cloning of cDNA encoding an unrecognized component of amyloid in Alzheimer disease. 1993;90:11282-6.
[16] Polymeropoulos MH, Lavedan C, Leroy E, Ide SE, Dehejia A, Dutra A, et al. Mutation in the α-synuclein gene identified in families with Parkinson's disease. 1997;276:2045-7.
[17] Davidson WS, Jonas A, Clayton DF, George JMJJoBC. Stabilization of α-synuclein secondary structure upon binding to synthetic membranes. 1998;273:9443-9.
[18] Pfefferkorn CM, Jiang Z, Lee JCJBeBA-B. Biophysics of α-synuclein membrane interactions. 2012;1818:162-71.
[19] Spillantini MG, Crowther RA, Jakes R, Cairns NJ, Lantos PL, Goedert MJNl. Filamentous α-synuclein inclusions link multiple system atrophy with Parkinson's disease and dementia with Lewy bodies. 1998;251:205-8.
[20] Wang L, Das U, Scott DA, Tang Y, McLean PJ, Roy SJCB. α-synuclein multimers cluster synaptic vesicles and attenuate recycling. 2014;24:2319-26.
[21] Abeliovich A, Schmitz Y, Fariñas I, Choi-Lundberg D, Ho W-H, Castillo PE, et al. Mice lacking α-synuclein display functional deficits in the nigrostriatal dopamine system. 2000;25:239-52.
[22] Scialò C, De Cecco E, Manganotti P, Legname GJV. Prion and prion-like protein strains: deciphering the molecular basis of heterogeneity in neurodegeneration. 2019;11:261.
[23] Stadtman ER, Berlett BSJCrit. Reactive oxygen-mediated protein oxidation in aging and disease. 1997;10:485-94.
[24] Boveris A, Oshino N, Chance BJBJ. The cellular production of hydrogen peroxide. 1972;128:617-30.
[25] Fujiwara H, Hasegawa M, Dohmae N, Kawashima A, Masliah E, Goldberg MS, et al. α-Synuclein is phosphorylated in synucleinopathy lesions. 2002;4:160-4.

[26] Paleologou KE, Oueslati A, Shakked G, Rospigliosi CC, Kim H-Y, Lamberto GR, et al. Phosphorylation at S87 is enhanced in synucleinopathies, inhibits α-synuclein oligomerization, and influences synuclein-membrane interactions. 2010;30:3184-98.
[27] Nakamura T, Yamashita H, Nagano Y, Takahashi T, Avraham S, Avraham H, et al. Activation of Pyk2/RAFTK induces tyrosine phosphorylation of α-synuclein via Src-family kinases. 2002;521:190-4.
[28] Hokenson MJ, Uversky VN, Goers J, Yamin G, Munishkina LA, Fink ALJB. Role of individual methionines in the fibrillation of methionine-oxidized α-synuclein. 2004;43:4621-33.
[29] Peelaerts W, Baekelandt VJJon. α-Synuclein strains and the variable pathologies of synucleinopathies. 2016;139:256-74.
[30] Baldwin AJ, Knowles TP, Tartaglia GG, Fitzpatrick AW, Devlin GL, Shammas SL, et al. Metastability of native proteins and the phenomenon of amyloid formation. 2011;133:14160-3.
[31] Guerrero-Ferreira R, Taylor NM, Mona D, Ringler P, Lauer ME, Riek R, et al. Cryo-EM structure of alpha-synuclein fibrils. 2018;7:e36402.
[32] Dearborn AD, Wall JS, Cheng N, Heymann JB, Kajava AV, Varkey J, et al. α-Synuclein amyloid fibrils with two entwined, asymmetrically associated protofibrils. 2016;291:2310-8.
[33] Der-Sarkissian A, Jao CC, Chen J, Langen RJJoBC. Structural organization of α-synuclein fibrils studied by site-directed spin labeling. 2003;278:37530-5.
[34] Kessler JC, Rochet J-C, Lansbury PTJB. The N-terminal repeat domain of α-synuclein inhibits β-sheet and amyloid fibril formation. 2003;42:672-8.
[35] Shen N, Song G, Yang H, Lin X, Brown B, Hong Y, et al. Identifying the pathological domain of alpha-synuclein as a therapeutic for parkinson's disease. 2019;20:2338.
[36] Giasson BI, Murray IV, Trojanowski JQ, Lee VM-YJJoBC. A hydrophobic stretch of 12 amino acid residues in the middle of α-synuclein is essential for filament assembly. 2001;276:2380-6.
[37] Du H-N, Tang L, Luo X-Y, Li H-T, Hu J, Zhou J-W, et al. A peptide motif consisting of glycine, alanine, and valine is required for the fibrillization and cytotoxicity of human α-synuclein. 2003;42:8870-8.
[38] Heise H, Hoyer W, Becker S, Andronesi OC, Riedel D, Baldus MJPotNAoS. Molecular-level secondary structure, polymorphism, and dynamics of full-length α-synuclein fibrils studied by solid-state NMR. 2005;102:15871-6.
[39] Guan Y, Zhao X, Liu F, Yan S, Wang Y, Du C, et al. Pathogenic Mutations Differentially Regulate Cell-to-Cell Transmission of α-Synuclein. 2020;14:159.
[40] Sipe JD, Cohen ASJJosb. History of the amyloid fibril. 2000;130:88-98.
[41] Snow AD, Sekiguchi RT, Nochlin D, Kalaria RN, Kimata KJTAjop. Heparan sulfate proteoglycan in diffuse plaques of hippocampus but not of cerebellum in Alzheimer's disease brain. 1994;144:337.
[42] Goedert M, Jakes R, Spillantini M, Hasegawa M, Smith M, Crowther RJN. Assembly of microtubule-associated protein tau into Alzheimer-like filaments induced by sulphated glycosaminoglycans. 1996;383:550-3.
[43] Pérez M, Valpuesta JM, Medina M, Montejo de Garcini E, Avila JJJon. Polymerization of τ into filaments in the presence of heparin: the minimal sequence required for τ-τ interaction. 1996;67:1183-90.
[44] Snow AD, Willmer JP, Kisilevsky RJHp. Sulfated glycosaminoglycans in Alzheimer's disease. 1987;18:506-10.
[45] Snow AD, Kisilevsky R, Willmer J, Prusiner S, DeArmond SJAn. Sulfated glycosaminoglycans in amyloid plaques of prion diseases. 1989;77:337-42.
[46] Perry G, Richey P, Siedlak SL, Galloway P, Kawai M, Cras PJBr. Basic fibroblast growth factor binds to filamentous inclusions of neurodegenerative diseases. 1992;579:350-2.
[47] Friedhoff P, Schneider A, Mandelkow E-M, Mandelkow EJB. Rapid assembly of Alzheimer-like paired helical filaments from microtubule-associated protein tau monitored by fluorescence in solution. 1998;37:10223-30.
[48] Castillo GM, Lukito W, Wight TN, Snow ADJJon. The sulfate moieties of glycosaminoglycans are critical for the enhancement of β-amyloid protein fibril formation. 1999;72:1681-7.
[49] Capila I, Linhardt RJJACIE. Heparin–protein interactions. 2002;41:390-412.
[50] Nishitsuji K, Uchimura KJGJ. Sulfated glycosaminoglycans in protein aggregation diseases. 2017;34:453-66.

[51] Hileman RE, Fromm JR, Weiler JM, Linhardt RJJB. Glycosaminoglycan-protein interactions: definition of consensus sites in glycosaminoglycan binding proteins. 1998;20:156-67.
[52] Soares da Costa D, Reis RL, Pashkuleva IJArobe. Sulfation of glycosaminoglycans and its implications in human health and disorders. 2017;19:1-26.
[53] Holmes BB, DeVos SL, Kfoury N, Li M, Jacks R, Yanamandra K, et al. Heparan sulfate proteoglycans mediate internalization and propagation of specific proteopathic seeds. 2013;110:E3138-E47.
[54] Bieri G, Gitler AD, Brahic MJNod. Internalization, axonal transport and release of fibrillar forms of alpha-synuclein. 2018;109:219-25.
[55] Ihse E, Yamakado H, van Wijk XM, Lawrence R, Esko JD, Masliah EJSr. Cellular internalization of alpha-synuclein aggregates by cell surface heparan sulfate depends on aggregate conformation and cell type. 2017;7:1-10.
[56] Feyzi E, Saldeen T, Larsson E, Lindahl U, Salmivirta MJJoBC. Age-dependent modulation of heparan sulfate structure and function. 1998;273:13395-8.
[57] Mehra S, Ghosh D, Kumar R, Mondal M, Gadhe LG, Das S, et al. Glycosaminoglycans have variable effects on α-synuclein aggregation and differentially affect the activities of the resulting amyloid fibrils. 2018;293:12975-91.
[58] Cohlberg JA, Li J, Uversky VN, Fink ALJB. Heparin and other glycosaminoglycans stimulate the formation of amyloid fibrils from α-synuclein in vitro. 2002;41:1502-11.
[59] Trexler AJ, Rhoades EJBj. Single molecule characterization of α-synuclein in aggregation-prone states. 2010;99:3048-55.
[60] Madine J, Clayton JC, Yates EA, Middleton DAJO, chemistry b. Exploiting a 13C-labelled heparin analogue for in situ solid-state NMR investigations of peptide-glycan interactions within amyloid fibrils. 2009;7:2414-20.
[61] Vilasi S, Sarcina R, Maritato R, De Simone A, Irace G, Sirangelo IJPo. Heparin induces harmless fibril formation in amyloidogenic W7FW14F apomyoglobin and amyloid aggregation in wild-type protein in vitro. 2011;6:e22076.
[62] Madine J, Davies HA, Hughes E, Middleton DAJB. Heparin promotes the rapid fibrillization of a peptide with low intrinsic amyloidogenicity. 2013;52:8984-92.
[63] Tria G, Mertens HD, Kachala M, Svergun DIJI. Advanced ensemble modelling of flexible macromolecules using X-ray solution scattering. 2015;2:207-17.
[64] Vranken WF, Boucher W, Stevens TJ, Fogh RH, Pajon A, Llinas M, et al. The CCPN data model for NMR spectroscopy: development of a software pipeline. 2005;59:687-96.
[65] Bertoncini CW, Jung Y-S, Fernandez CO, Hoyer W, Griesinger C, Jovin TM, et al. Release of long-range tertiary interactions potentiates aggregation of natively unstructured α-synuclein. 2005;102:1430-5.
[66] Nygaard M, Kragelund BB, Papaleo E, Lindorff-Larsen KJBj. An efficient method for estimating the hydrodynamic radius of disordered protein conformations. 2017;113:550-7.
[67] Skolnick J, Kolinski A, Ortiz ARJJomb. MONSSTER: a method for folding globular proteins with a small number of distance restraints. 1997;265:217-41.
[68] Kohn JE, Millett IS, Jacob J, Zagrovic B, Dillon TM, Cingel N, et al. Random-coil behavior and the dimensions of chemically unfolded proteins. 2004;101:12491-6.
[69] Van Maarschalkerweerd A, Pedersen M, Peterson H, Nilsson M, Nguyen T, Skamris T, et al. Formation of covalent di-tyrosine dimers in recombinant α-synuclein. 2015;3:e1071302.
[70] Wilkins DK, Grimshaw SB, Receveur V, Dobson CM, Jones JA, Smith LJJB. Hydrodynamic radii of native and denatured proteins measured by pulse field gradient NMR techniques. 1999;38:16424-31.
[71] Marsh JA, Forman-Kay JDJBj. Sequence determinants of compaction in intrinsically disordered proteins. 2010;98:2383-90.
[72] Skaanning LK, Santoro A, Skamris T, Martinsen JH, D'Ursi AM, Bucciarelli S, et al. The Non-Fibrillating N-Terminal of α-Synuclein Binds and Co-Fibrillates with Heparin. 2020;10:1192.
[73] Teilum K, Kunze MBA, Erlendsson S, Kragelund BBJPS. (S) Pinning down protein interactions by NMR. 2017;26:436-51.
[74] Prestel A, Wichmann N, Martins JM, Marabini R, Kassem N, Broendum SS, et al. The PCNA interaction motifs revisited: thinking outside the PIP-box. 2019;76:4923-43.

[75] Blanchet CE, Spilotros A, Schwemmer F, Graewert MA, Kikhney A, Jeffries CM, et al. Versatile sample environments and automation for biological solution X-ray scattering experiments at the P12 beamline (PETRA III, DESY). 2015;48:431-43.
[76] Franke D, Kikhney AG, Svergun DIJNI, Methods in Physics Research Section A: Accelerators S, Detectors, Equipment A. Automated acquisition and analysis of small angle X-ray scattering data. 2012;689:52-9.
[77] Konarev PV, Volkov VV, Sokolova AV, Koch MH, Svergun DIJJoac. PRIMUS: a Windows PC-based system for small-angle scattering data analysis. 2003;36:1277-82.
[78] Cholak E, Bucciarelli S, Bugge K, Johansen NT, Vestergaard B, Arleth L, et al. Distinct α-synuclein: lipid co-structure complexes affect amyloid nucleation through fibril mimetic behavior. 2019;58:5052-65.
[79] Orekhov VY, Jaravine VAJPinmrs. Analysis of non-uniformly sampled spectra with multi-dimensional decomposition. 2011;59:271-92.
[80] Stilbs PJAC. Molecular self-diffusion coefficients in Fourier transform nuclear magnetic resonance spectrometric analysis of complex mixtures. 1981;53:2135-7.
[81] Stejskal EO, Tanner JEJTjocp. Spin diffusion measurements: spin echoes in the presence of a time-dependent field gradient. 1965;42:288-92.
[82] Schwarzinger S, Kroon GJ, Foss TR, Chung J, Wright PE, Dyson HJJJotACS. Sequence-dependent correction of random coil NMR chemical shifts. 2001;123:2970-8.
[83] Kjaergaard M, Brander S, Poulsen FMJJobN. Random coil chemical shift for intrinsically disordered proteins: effects of temperature and pH. 2011;49:139-49.
[84] Kjaergaard M, Poulsen FMJJobN. Sequence correction of random coil chemical shifts: correlation between neighbor correction factors and changes in the Ramachandran distribution. 2011;50:157-65.